이학박사 학위논문

Study of wide bandgap oxide semiconductors, SnO_2 and $ZnGa_2O_4$, using thin film transistors

박막 트랜지스터를 이용한 넓은 밴드갭 산화물 반도체 SnO_2, $ZnGa_2O_4$ 연구

2020 년 08 월

서울대학교 대학원

물리·천문학부

장 예 주

Study of wide bandgap oxide semiconductors, SnO_2 and $ZnGa_2O_4$, using thin film transistors

지도 교수 차 국 린

이 논문을 이학박사 학위논문으로 제출함
2020 년 06 월

서울대학교 대학원
물리·천문학부
장 예 주

장예주의 이학박사 학위논문을 인준함
2020 년 07 월

위 원 장 이탁희 (인)

부위원장 차국린 (인)

위 원 전헌수 (인)

위 원 박 윤 (인)

위 원 이기영 (인)

Abstract

Study of wide bandgap oxide semiconductors, SnO_2 and $ZnGa_2O_4$, using thin film transistors

Yeaju Jang

Department of Physics and Astronomy

The Graduate School

Seoul National University

This dissertation focused on the study of wide bandgap oxide semiconductors, SnO_2 and $ZnGa_2O_4$, using thin film transistors. To investigate the material properties and potential to visible/UV transparent and high power devices, thin films and thin film transistors were exploited. Especially, using thin film transistors has the advantages of not only demonstrating device performance but also investigating material electric transport properties by modulating carriers with the electric field.

Semiconductor materials which have larger bandgap than conventional semiconductors, such as Si and GaAs (bandgap, E_g: 1 ~ 1.5 eV), are called as wide bandgap semiconductors. With the larger bandgap than the visible range of 3.1 eV, the semiconductor materials are transparent in the visible range. The materials are transparent in ultraviolet A (UVA: 3.1 ~ 3.94 eV) and ultraviolet B (UVB: 3.94 ~ 4.43 eV) with the bandgap over 3.94 eV and 4.43 eV, respectively. Moreover, the wider bandgap materials have a higher breakdown field strength because the electric field to generate and accelerate carriers become large as increasing bandgap. With

these properties, wide bandgap semiconductors are particularly important for display/optoelectronics and high power devices due to their transparency and high breakdown field. The known wide bandgap semiconductors are IGZO (E_g = 3.0 eV), $BaSnO_3$ (E_g = 3.1 eV), ZnO (E_g = 3.3 eV), SiC (E_g = 3.3 eV), SnO_2 (E_g = 3.6 eV), $SrSnO_3$ (E_g = 4.6 eV), β-Ga_2O_3 (E_g = 4.8 ~ 4.9 eV), $ZnGa_2O_4$ (E_g = 4.6 ~ 5.2 eV), $Al_xGa_{1-x}N$ (E_g = 3.4 ~ 6.0 eV), and diamond (E_g = 5.5 eV).

SnO_2 is a transparent semiconductor with a wide bandgap of 3.6 eV. Despite the difficulty of transparency and conduction coexistence, SnO_2 shows optical transparency and conductive electric properties at the same time. SnO_2 exhibits the 97 % transmittance in the visible range. Depending on crystallinity and doping concentration, SnO_2 has a resistivity of 10^{-4} ~ 10^6 Ω·cm (most semiconductor 10^{-3} ~ 10^9 Ω·cm) and carrier concentration of 10^{17} ~ 10^{20} cm^{-3} with high mobility. From these properties, SnO_2 can be used not only for a transparent conductive oxide (TCO) but also for a transparent oxide semiconductor (TOS). As a TCO, SnO_2 is widely used to solar cell and flat panel display in itself or alloy with In_2O_3. Due to its electrical transport properties and transparency along with thermal and chemical stability, SnO_2 is one of the promising TOS candidates especially for replacing IGZO at the display industry.

The transparent thin film transistors (TFTs) based on polycrystalline SnO_2 and epitaxial SnO_2 were fabricated and compared. Reactive sputtering methods and subsequent annealing process were used for polycrystalline SnO_2 deposition on the glass. Both top and bottom gate geometry TFTs of polycrystalline SnO_2 showed high mobility of 145.7 cm^2/Vs and 160.0 cm^2/Vs, respectively. However, the polycrystalline SnO_2 TFTs exhibited the non-ideal characteristics in output and transfer characteristics; a large hysteresis along with voltage dependence. The probable origin of these behaviors is the barrier formation across polycrystalline SnO_2 grains. To confirm this, epitaxial SnO_2 TFTs were fabricated on r plane sapphire (r-Al_2O_3) by a pulsed laser deposition method. Although the mobility of epitaxial SnO_2 TFT was not as high as that of polycrystalline SnO_2 TFT, non-ideal behaviors disappeared. By comparing TFTs characteristics and structural properties,

it was confirmed that grain boundaries of polycrystalline SnO_2 cause the unstable TFT characteristics and high density of threading dislocations and antiphase boundaries are the origins of the low mobility of epitaxial SnO_2 TFT. The use of polycrystalline SnO_{2-x} TFTs will require a thorough understanding of grain boundaries.

Normal spinel oxide $ZnGa_2O_4$ (ZGO) is known as having an ultra-wide bandgap of 4.6 ~ 5.2 eV and transparency in UV region. ZGO has two cations of Zn^{2+} at the tetrahedral site and Ga^{3+} at the octahedral site along with the GaO_6 octahedra network as β-Ga_2O_3. ZGO is expected to possess strengths over β-Ga_2O_3. From a normal cubic spinel structure, ZGO shows isotropic properties and stable phase. ZGO has higher conductivity and doping possibility than β-Ga_2O_3 due to its normal spinel phase with two cation sites. Based on these strengths, ZGO is spotlighted as a high power device and UV transparent device candidate.

The coherent epitaxial $ZnGa_2O_4$(ZGO) layers were grown on $MgAl_2O_4$ and MgO substrates by pulsed laser deposition. Using X-ray diffraction and transmission electron microscopy, it was confirmed that the ZGO is a spinel structure without any threading/misfit dislocations. Depending on the strains (compressive or tensile strain) by substrates and cations (Zn^{2+}, Ga^{3+}) compositional ratio, the ZGO thin films and TFTs exhibited different structural and electric transport properties. When the Zn/Ga ratio is slightly lower than the ideal value of 0.5 with tensile strain, the ZGO TFT showed the highest mobility of 5.4 cm^2/Vs, a large I_{ON}/I_{OFF} ratio of 4.5×10^8, and small subthreshold swing value of 0.19 V/dec. From the structural and electrical characteristics of the ZGO thin films and ZGO TFTs, Zn vacancies and antisite defects of Ga located at Zn site seem to be the dominant defects of the ZGO. Further understanding of ZGO defects and strain will improve TFTs performances.

Keywords: Wide bandgap oxide semiconductor, SnO_2, $ZnGa_2O_4$, Thin film, Thin film transistor

Student number: 2013-22994

Contents

List of Figures

List of Tables

Chapter 1. Introduction

1.1 Wide bandgap semiconductors

With the larger bandgap compared to the conventional semiconductors of Si and GaAs (E_g: 1 ~ 1.5 eV), wide bandgap semiconductors show two prominent strengths over conventional semiconductors. The strengths are visible/ultraviolet (UV) transparency and high breakdown field. As shown in Figure 1.1, the well known wide bandgap semiconductors are IGZO (E_g = 3.0 eV) [1], $BaSnO_3$ (E_g = 3.1 eV) [2], ZnO (E_g = 3.3 eV) [3], SiC (E_g = 3.3 eV) [4], SnO_2 [5], $SrSnO_3$ (E_g = 4.6 eV) [6], β-Ga_2O_3 (E_g = 4.8 ~ 4.9 eV) [4, 7], $ZnGa_2O_4$ [8-10], $Al_xGa_{1-x}N$ (E_g = 3.4 ~ 6.0 eV) [4], and diamond (E_g = 5.5 eV) [4].

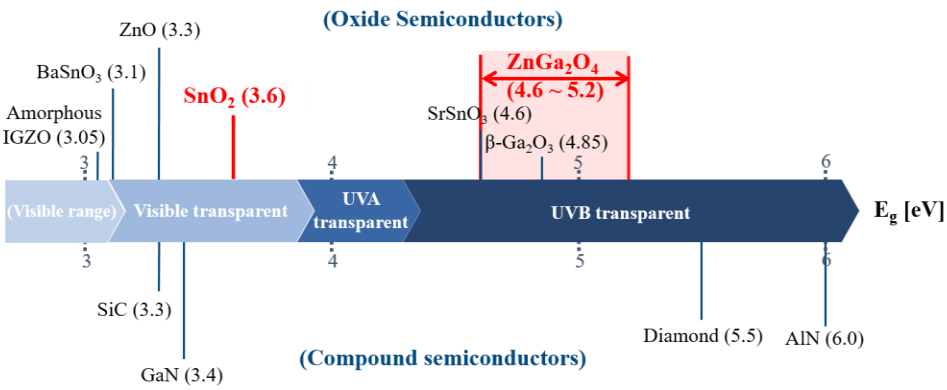

Figure 1.1.Wide bandgap semiconductors [1-10].

Since the visible range is 1.65 ~ 3.1 eV (corresponding wavelength: 740 ~ 380 nm), wide bandgap semiconductors with larger bandgap than 3.1 eV are optically transparent. Generally, high optical transparency is incompatible with high electrical conduction because doping and carrier generation become difficult as larger bandgap. In this regard, transparent conductive oxide (TCO) materials are exceptional. [11] TCOs are importantly considered in the displays, light-emitting diodes (LEDs), and photovoltaics applications. For these applications, TCOs are usually used as transparent electrodes without blocking light. The commonly used TCOs are indium tin oxide (ITO) and fluorine-doped tin oxide (FTO), and ZnO. The development of TCO and the increasing requirement for transparent optoelectronics devices which could not be covered by hydrogenated amorphous Si (a-Si:H) cause the attention to transparent oxide semiconductors (TOS). The most investigated TOS are a-IGZO (amorphous IGZO), ZnO, and SnO_2. Among them, although a-IGZO based TFTs have been used for displays with high mobility, a-IGZO has a disadvantage of expansive indium. In this dissertation, TFTs of SnO_2 (E_g: 3.6 eV) possessing a wide range of carrier density with high mobility is evaluated as the replacement of a-IGZO and the TOS candidate for transparent display/optoelectronics applications. [11]

Conventional TCO/TOS, such as ZnO and SnO_2, are opaque in the deep-ultraviolet (DUV, wavelength < 300 nm) region because of the relatively small bandgap. UV transparency is especially crucial not only for UV transparent optoelectronics devices but also for UV detectors of biological samples because DNA absorbing peaks are around 260 nm [12]. In this sense, ultra-wide bandgap semiconductors (E_g > 4.0 eV) become important and are attracting much scientific attention. The UV range is divided into three sections as ultraviolet A (UVA, 3.1 ~ 3.94 eV), ultraviolet B (UVB, 3.94 ~ 4.43 eV), and ultraviolet C (UVC, 4.43 ~ 12.4 eV). The larger bandgap semiconductors than 3.94 eV and 4.43 eV are transparent in UVA and UVB regions, respectively.

Besides UV transparency, ultra-wide bandgap semiconductors have a significant advantage of the high breakdown field. The wider bandgap semiconductor requires a higher electric field to generate carriers having enough kinetic energy for collisions

and breakdown. The known breakdown field strengths are 0.3 MV/cm for Si (E_g = 1.1 eV), 0.4 MV/cm for GaAs (E_g = 1.4 eV), 2.5 MV/cm for SiC (E_g = 3.3 eV), 3.3 MV/cm for GaN (E_g = 3.4 eV), 9 MV/cm (expected) for β-Ga_2O_3 (E_g = 4.8 ~ 4.9 eV), 10 MV/cm for diamond (E_g = 5.5 eV), and over 10 MV/cm for AlN (E_g = 6 eV), respectively [4, 12]. From the experimental data, the breakdown fields tend to be proportional to the square ~ cubic of the material bandgap (Figure 1.2 (a)) [13]. Owing to the high breakdown field, ultra-wide bandgap semiconductors have been investigated for high power devices dealing with high current and voltage. Baliga's figure of merit (BFOM) for high power device performance at low frequency characterizes the material parameters to reduce conduction losses. BFOM is defined as $\varepsilon\mu E_g^3$ or V_{BR}^2/R_{ON} where ε is the dielectric constant of semiconductor, μ is mobility, E_g is bandgap, V_{BR} is breakdown voltage (the maximum voltage that switch can block when it is off), and R_{ON} is specific on-resistance [4, 14]. Therefore, the higher the BFOM means the higher voltage that the device can block when off and/or the higher conductivity per unit area when on. Figure 1.2 (b) shows the BFOM contours of several wide bandgap and ultra-wide bandgap semiconductors.

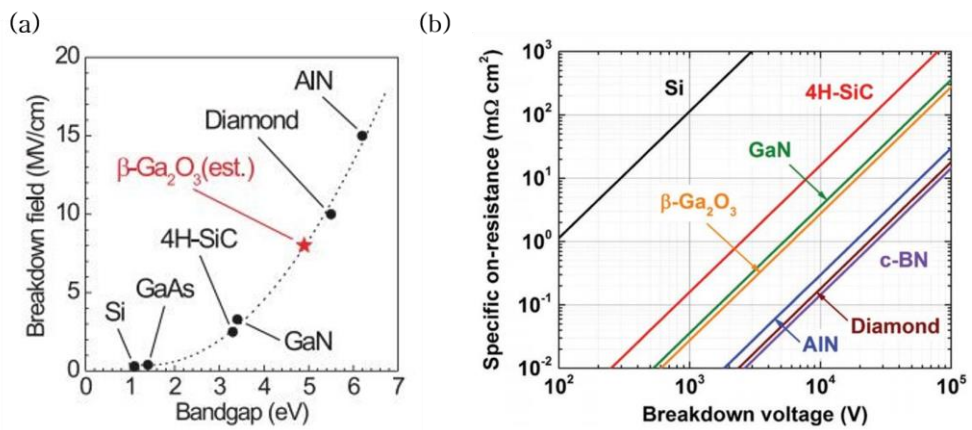

Figure 1.2. (a) Bandgap dependences of the breakdown field [13]. (b) BFOM contours of various semiconductors [4].

To date, the focus of intense investigation on the ultra-wide bandgap semiconductor materials has been $Al_xGa_{1-x}N$ (E_g = 3.4 ~ 6 eV)/AlN, diamond (E_g = 5.5 eV), and β-Ga_2O_3 (E_g = 4.8 ~ 4.9 eV) although a perovskite oxide $SrSnO_3$ (E_g = 4.6 eV) is emerging. Based on high breakdown field and UV transparency, the ultra-wide bandgap semiconductors show the distinguished properties depending on materials.

Since epitaxial GaN growth on sapphire substrates became possible, AlGaN/GaN HEMT (high electron mobility transistor) was demonstrated and GaN-based transistors have been intensively studied for high power devices [15]. Along with high mobility, the AlGaN alloys have good properties of direct bandgap reaching wide range, high saturation velocity (> 10^7 cm/s), and relative ease at being doped with Si. However, $Al_xGa_{1-x}N$/AlN is facing the problems of over doping, the absence of readily available single-crystal substrate, and the lack of scientific understanding for heteroepitaxy control. [4, 16-19]

Diamond has the outstanding properties of high electron and hole mobility (> 3000 cm^2/Vs) [20], high saturation drift velocity (2.3×10^7 cm/s for electrons, 1.4×10^7 cm/s for holes) [4], and the highest thermal conductivity (> 2000 W/mK) among the known materials [21]. Especially, high thermal conductivity is crucial because performances of power electronics and optoelectronics devices are limited by heat removal. Despite these remarkable properties, diamond is facing the challenges of doping. It was proved that boron and phosphorus act as p-type dopant and n-type dopant, respectively. However, the dopants have high activation energy and low activated fraction, making it hard to demonstrate devices because of the difficulty of selective doping and contact. Besides the doping problem, the absence of large-area single-crystal, unstable dielectric interface (due to small affinity), insufficient understanding of heterostructure formation, and expensive prices are other problems of diamond. [4, 21]

Among the ultra-wide bandgap oxide candidates, monoclinic β-Ga_2O_3 is being currently actively investigated due to its materials properties and the availability of affordable large-area single-crystal substrates. β-Ga_2O_3 exhibits the controllability

of n-type doping and tunable resistivity (10^{-3} ~ 10^{12} Ω·cm) with Si and Sn dopants [22]. From the affordable large-area substrates, β-Ga_2O_3 has the considerable advantage of the low price benefit over AlGaN alloys and diamond. However, β-Ga_2O_3 has drawbacks of the absence of p-type doping, polymorphs of Ga_2O_3, and anisotropic optical, thermal, structural, and mechanical properties including easy cleaving. [4, 23]

Recently, $ZnGa_2O_4$ (ZGO) is newly spotlighted as ultra-wide bandgap semiconductor which is expected to have the advantages over β-Ga_2O_3. Normal spinel ZGO which has a bandgap of 4.6 ~ 5.2 eV is transparent in the DUV regime. With the hydrogen doping, ZGO electrical properties were scarcely investigated as transparent conductive oxide [24]. Recently, bulk ZGO single crystals and corresponding wafers for epitaxy were successfully prepared, and their electrical properties were reported [8]. From the cubic crystal, higher electrical conductivity, and distinct two cation sites of ZGO, ZGO is expected to show the properties over β-Ga_2O_3. In this dissertation, ZGO properties are also investigated for evaluating the ZGO potential as high power devices along with UV transparent applications.

1.2 Thin film transistor

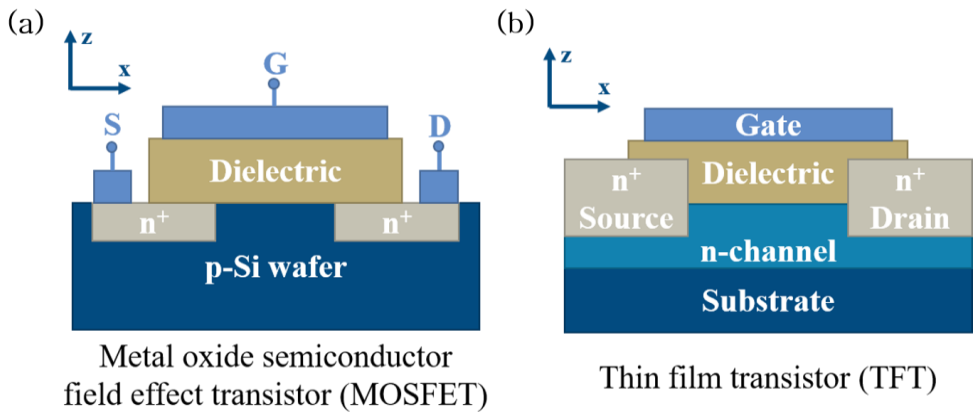

Figure 1.3. (a) A schematic of n-type metal oxide semiconductor field effect transistor (MOSFET). (b) A schematic of n-type thin film transistor (TFT).

The distinguishable difference of thin film transistor (TFT) from a conventional metal oxide semiconductor field effect transistor (MOSFET) is that the semiconductor materials are a thin film layer for TFT and Si wafer for MOSFET, respectively. The schematics of MOSFET and TFT are shown in Figure 1.3. The operation principle of TFT is similar to MOSFET except for the subtle differences [25, 26]. Here, the TFT operation mechanism is qualitatively and quantitatively explained by comparing it with the MOSFET operation fundamentals.

If positive gate bias V_{GS} is applied, electrons accumulated and rasing the channel conductance. With the negative V_{GS}, electrons are pushed away and lowering the channel conductance. Under the circumstance, the channel conductance behavior is different depending on n-type TFT or n-type MOSFET. While n-type TFT channel is n-type semiconductor layer, n-type MOSFET channel is p-doped wafer and source-drain contacts are the degenerated n-doped. It leads to accumulating holes into the channel layer and the channel conductance may not be low as much as n-

type TFT. It means that hole accumulation under negative V_{GS} occurs only in n-type MOSFET, not in n-type TFT. Except for this, the n-type TFT operation principle could be explained by n-type MOSFET operation principle under positive V_{GS}.

To specifically understand how the drain current is expected as changing applied voltage, set the source-drain voltage V_{DS} = 0 V and vary the V_{GS} (positive) for n-type MOSFET. When $V_{GS} \leq V_T$ (accumulation or depletion bias, where V_T is the depletion-inversion transition point voltage), the region between the source and drain contains either excess or deficient holes with few electrons. As $V_{GS} > V_T$ (inversion bias), the region consists of mobile electrons and becomes the n-type region (the inversion layer). As applying higher V_{GS}, the more electrons exist at the inversion layer, increasing the conductance of the region.

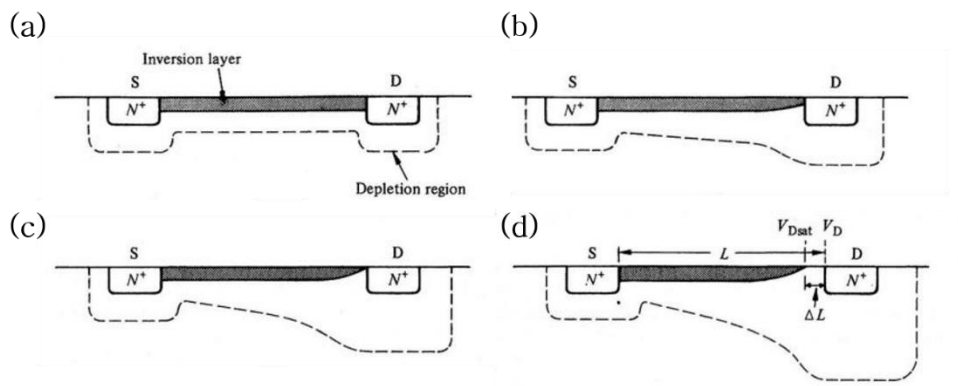

Figure 1.4. $V_{GS} > V_T$ (inversion bias) MOSFET operation modes. (a) V_{DS} = 0 V, (b) V_{DS} = moderate biasing, (c) pinch-off, and (d) after pinch-off. [25]

Next, consider raising the drain voltage step by step from V_{DS} = 0 V with the applying $V_{GS} > V_T$ (inversion bias). The inversion layer is thermal equilibrium and the drain current (I_{DS}) is zero at V_{DS} = 0 (Figure 1.4 (a)). With increase V_{DS}, the current(I_{DS}) flowing channel (inversion layer) increases until the channel becoming narrow. Continuing to increase the V_{DS} causes a reduction in the channel carrier concentration and induces a shrink of inversion layer near the drain as shown in

Figure 1.4 (b). Under high V_{DS} enough to vanish the inversion layer vicinity of the drain, the current saturates and it is called "pinch-off" (Figure 1.3 (c)).

To a quantitative explanation of the principles, consider the current density $\vec{J}$ when applying positive V_{GS}. The current density can be written as

$$\vec{J} = q\mu n\vec{E} + qD\vec{\nabla}n \tag{1.1}$$

where $q, \mu, n, \vec{E}$, and D are electron charge, mobility, carrier density, electric field, and diffusion coefficient, respectively. With positive V_{DS}, $\vec{J}$ is in the x-direction (Figure 1.3) and diffusion current is negligible because drift current is dominant on the entire channel. Therefore, equation (1.1) becomes

$$J_x \approx q\mu n E_x = -q\mu n \frac{d\phi}{dx} \tag{1.2}$$

where ϕ is an electrical potential. I_{DS} could be obtained from equation (1.2).

$$\begin{aligned} I_{DS} &= -\iint J_x dydz = -W\int_{-t}^{0} J_x dz \\ &= \left(-W\frac{d\phi}{dx}\right)\left(-q\int_{-t}^{0}\mu(x,z)n(x,z)dz\right) \end{aligned} \tag{1.3}$$

W and t are the width and thickness of the channel, respectively. 0 in the z-direction is set to be the interface between the channel and the dielectric. Because of narrowing the channel thickness, $\frac{d\phi}{dx}$ in equation (1.3) is regarded as constant. To integrate the right-hand side of equation (1.3), introduce the average mobility $\bar{\mu}$, n_{2D}

$$\bar{\mu} = \frac{\int_{-t}^{0}\mu(x,z)n(x,z)da}{\int_{-t}^{0}n(x,z)dz}\ ,\ n_{2D} = \int_{-t}^{0}n(x,z)dz \tag{1.4}$$

Therefore, equation (1.3) becomes

$$I_{DS} = W\bar{\mu}qn_{2D}\frac{d\phi}{dx} \tag{1.5}$$

Since I_{DS} is independent of x, integration of I_{DS} in equation (1.5) over the channel length L gives

$$I_{DS}L \approx W\bar{\mu}\int_0^{V_{DS}} qn_{2D}d\phi. \quad (1.6)$$

Assuming $\bar{\mu}$ is independent of x and considering gate electrode-dielectric-channel as a capacitor. Then, qn_{2D} in equation (1.5) can be written as

$$qn_{2D} = C\Delta V = C(V_{GS} - V_T - \phi) \quad (1.7)$$

where C is the capacitance per unit area of the dielectric. Using $C = \varepsilon/d$ (ε: the dielectric constant, d: dielectric thickness), substitutes equation (1.7) into equation (1.6).

$$I_{DS} = \frac{W\bar{\mu}\varepsilon}{Ld}\left[(V_{GS} - V_T)V_{DS} - \frac{V_{DS}^2}{2}\right] \quad (1.8)$$

The above equation is obtained with the assumption of electron accumulation layer formation throughout the entire channel. The assumption is only valid until before pinch-off ($0 \leq V_{DS} \leq V_{DS(saturation)}$, $V_{GS} \geq V_T$). After the pinch-off, I_{DS} is approximately constant if V_{DS} exceeds $V_{DS(saturation)}$ and pinch-off implies $qn_{2D}(x = L) \rightarrow 0$ when $V_{DS} \rightarrow V_{DS(saturation)}$. Therefore,

$$qn_{2D} = C(V_{GS} - V_T - \phi) = 0, V_{DS(saturation)} = V_{GS} - V_T \quad (1.9)$$

$$I_{DS(saturation)} = \frac{W\bar{\mu}\varepsilon}{2Ld}(V_{GS} - V_T)^2 \quad (1.10)$$

Neglecting average mobility's dependence on V_{GS}, equation (1.10) predicts a $I_{DS(saturation)}$ that varies as the square of the V_{GS} above turn-on. That is why this law is the so-called "square-law theory".

Figure 1.5 shows the output and transfer characteristics of general n-type TFT or MOSFET. From square-law theory, the average mobility ($\bar{\mu}$) is called a field effect mobility (μ_{FE}) and can be extracted transfer characteristics at $V_{DS} < V_{DS(saturation)}$ (linear region) as

$$\mu_{FE} = \frac{Ld}{W\varepsilon V_{DS}}\left(\frac{\partial I_{DS}}{\partial V_{GS}}\right). \quad (1.11)$$

The maximum field effect mobility is presented as a parameter of device evaluation.

The other evaluation parameters are subthreshold swing (S) and I_{ON}/I_{OFF} ratio following as

$$S = \left(\frac{\partial log I_{DS}}{\partial V_{GS}}\right)^{-1} \tag{1.12}$$

$$\frac{I_{ON}}{I_{OFF}} ratio = \frac{maximum\ \ ON\ \ current}{minimum\ \ OFF\ \ current}. \tag{1.13}$$

Small S value means a high speed to turn on and low power consumption. Large I_{ON}/I_{OFF} ratio implies a high performance (high I_{ON}) and low leakage power (low I_{OFF}) for the device.

For MOSFET, it is known that the square-law theory overestimates $I_{DS(saturation)}$ and $V_{DS(saturation)}$ because the variation of depletion width depending on V_{DS} is neglected. To replace this, bulk-charge theory including space charges in the depletion region is used for MOSFET. However, in the case of TFT, it is not necessary to consider the bulk-charge theory because there is no or small depletion region.

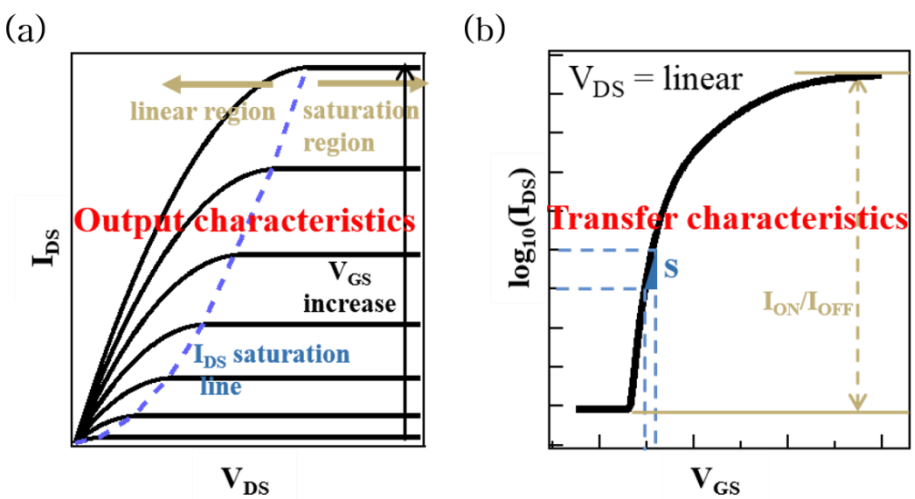

Figure 1.5. The general n-type TFT/MOSFET characteristics. (a) Output characteristics (I_{DS}-V_{DS} with V_{GS} increase step by step). (b) Transfer characteristics (I_{DS}-V_{GS} with fixed V_{DS}).

Chapter 2. Experimental methods and characteristics

2.1 Reactive magnetron sputtering: polycrystalline SnO_2

Sputtering is widely used for planar thin film growth. Understanding the sputtering principle is based on plasma which is the ionized gas state. For sputtering, argon is usually used to generate plasma. By applying an electrical current between two electrodes within a magnetic field, the plasma is generated. The ionized argon is accelerated by the electric field. The accelerated argon-ion collides with the target. In this collision, when the argon-ion kinetic energy is higher than the self-bonding energy of the target material, the bonding breaks off and the elements composing the target go to the substrate with kinetic energy.

For SnO_2 deposition, 99.999 % Sn metal target was used and the Sn oxidization occurs by inserting oxygen gas during the process. That is why this process is called reactive sputtering. Figure 2.1 shows this process. Polycrystalline SnO_2 deposition was proceeded at room temperature and using glass as a substrate. Depending on the total pressure and the composition ratio of the background atmosphere, polycrystalline SnO_2 exhibited different properties. Fixing total pressure 2 mTorr, the oxygen partial pressure was changed as O_2:Ar = 5:5, 7:3, and 9:1. The dc sputtering power was 40 W. The stencil masks made of SUS/Si were used to deposit the patterned SnO_2 layer for TFT fabrication. The SnO_2 thin films grown at room temperature were amorphous and almost insulating [27]. To crystallize and enhance the electrical properties, the films were annealed for an hour in a tube furnace at 400 ℃ with flowing oxygen in the atmosphere. The post-deposition annealing process was only for crystallization and enhancement of electrical properties and

made not the difference in polycrystalline SnO_2 thin film electrical properties depending on oxygen partial pressure during the deposition.

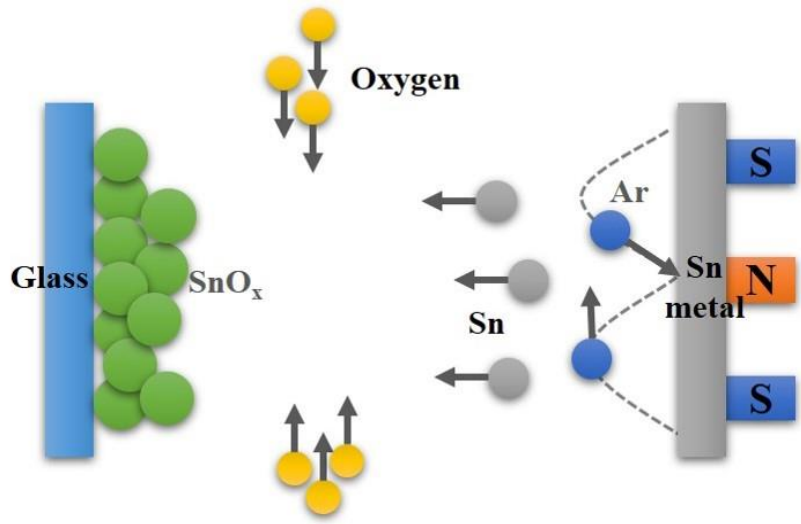

Figure 2.1. Illustration of the reactive sputtering process.

2.2 Pulsed laser deposition: epitaxial SnO_2, $ZnGa_2O_4$, and ITO

Epitaxial SnO_2, $ZnGa_2O_4$, and Sn-doped In_2O_3 (ITO) electrodes were deposited by pulsed laser deposition (PLD) method. PLD is one of the PVD techniques, where a high power pulsed laser beam is focused on a target material in a vacuum or in the presence of a background gas. When the intense pulsed laser is focused on a target, significant material removal from the target occurs in the form of the luminous plume containing separated ions with above a threshold power density depending on target materials. The plume propagates to a substrate while interacting with ambient gas. When the ions compositing target materials reach a substrate, the deposition occurs. Figure 2.2 shows this process schematically.

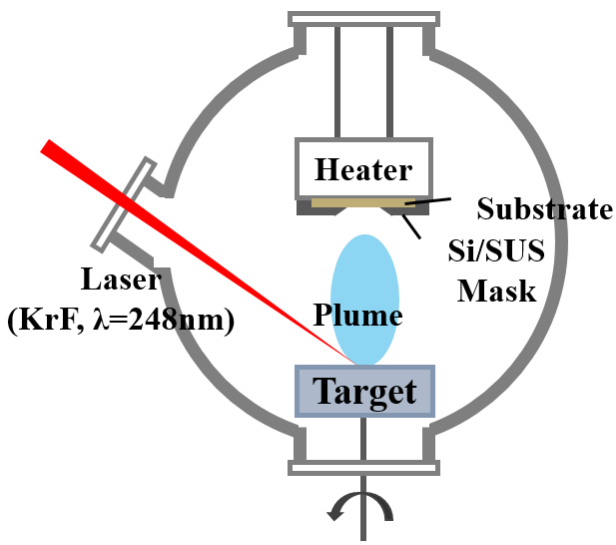

Figure 2.2. Illustration of the pulsed laser deposition (PLD) process.

In comparison with other methods, PLD has the advantage of controlling several parameters, such as target-substrate distance, focused laser spot (size, shape), laser frequency, laser energy, laser wavelength, background gas (pressure, gas type), and deposition temperature, which are crucial for crystallinity, uniformity, and stoichiometry of films. Especially, the focused laser spot is optimized by using aperture and controlling the distances from aperture to lens and from lens to target. The aperture ~ lens and lens ~ target distances are determined by lens focal length. Through the optimizing, the focused laser becomes uniform and generates uniform plume. In addition to the optimization of the focused laser beam, the uniform thin film is deposited by changing a target position with DC and step motors. Using the DC and step motors makes it possible for the sequential deposition with 2 ~ 3 targets. As controlling the parameters, the PLD method is easy and useful to the deposition of the stoichiometric sample.

The wavelength of the laser was 248 nm and the repetition rate was 1 ~ 10 Hz. The base pressure was 6 ~ 8 x 10^{-6} Torr. To fabricate TFT for each material, the stencil masks made of Si or SUS was used to deposit the patterned layer. The other conditions were different depending on the deposition materials.

Epitaxial SnO_2 was deposited by using a pulsed laser energy density of 1.3 ~ 1.5 J/cm^2 at 800 ℃. A 99.99 % ceramic SnO_2 target was used for the source material and r plane sapphire (r-Al_2O_3) was used as substrates. The distance between the target and substrate is about 4 cm. During the deposition, working pressure was oxygen 200 mTorr and 50 ~ 15 mTorr for insulating buffer layer and conducting layer, respectively. These conditions are based on the previous epitaxial SnO_2 study [28].

$ZnGa_2O_4$ (ZGO) was deposited by using a pulsed laser energy density of 1.3 J/cm^2. The distance between the targets and substrate was about 4 cm. As using different substrates, the different deposition conditions were used. On c plane sapphire (c-Al_2O_3) substrates, the deposition temperature was 750 ℃ and the working pressure was oxygen 100 mTorr. Due to the Zn volatility, the sequential deposition of Ga_2O_3 and ZnO ceramic targets was used by controlling pulse shot ratios of Ga_2O_3:ZnO =

4:30 ~ 40. When $MgAl_2O_4$ and MgO were used as substrates, the deposition temperature was 450 ℃ and the working pressure was oxygen 10 mTorr. Because of the volatility of Zn at high temperatures, more Zn was added by alternatively depositing from each of the $ZnGa_2O_4$ and ZnO ceramic targets. The control of the Zn ratio was achieved by the pulse shot ratio on the ZGO and ZnO targets; ZGO:ZnO pulse shot ratio was changed from 10:0 to 10:10. It was made sure that each cycle was smaller than the unit cell of ZGO. Figure 2.3 shows the pictures of plumes for each target of ZGO deposition.

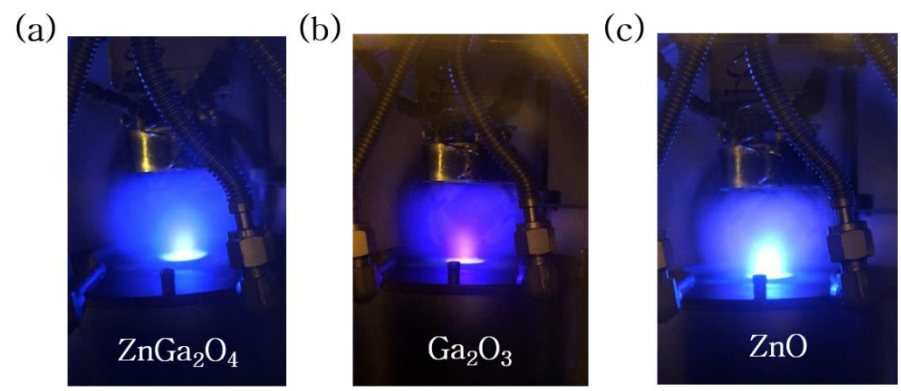

Figure 2.3. The pictures of the plume of (a) $ZnGa_2O_4$, (b) Ga_2O_3, and (c) ZnO.

Sn-doped In_2O_3 (ITO) deposited by PLD was used for electrodes of polycrystalline SnO_2, epitaxial SnO_2, and $ZnGa_2O_4$ TFTs. For ITO deposition, the deposition temperature, laser energy density, working pressure, and target-substrate distance were 150 ℃, 0.8 J/cm^2, oxygen 10 mTorr, and 6.5 ~ 7 cm, respectively. It was confirmed that ITO which was deposited under these conditions has a resistivity below 7×10^{-4} Ω·cm.

2.3 Atomic layer deposition: HfO_2 and Al_2O_3 gate dielectrics

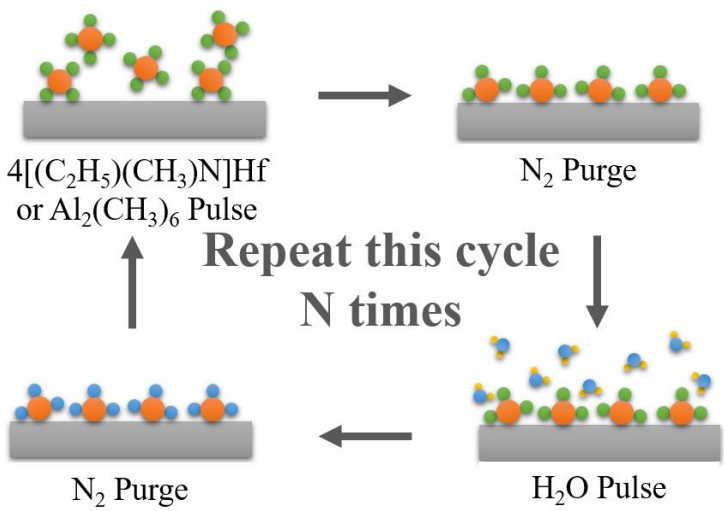

Figure 2.4. Illustration of atomic layer deposition (ALD).

Atomic layer deposition (ALD) is a subclass of a chemical vapor deposition (CVD) method which is based on the sequentially alternating pulse use of gas phase chemical precursors. During the ALD process, a thin film is grown on a substrate by exposing the surface to precursors. Unlike CVD, there is no simultaneous presence of precursors by inert gas purge as shown in Figure 2.4. Although the growth rate is different depending on deposition temperature and precursor-substrate surface interaction, the deposited thickness per one cycle is less than a monolayer (~ Å/cycle). ALD offers advantages of conformality on high aspect ratio structure, thickness control at the atomic level, adjustable film composition, and low leakage current [29].

ALD was used to grow gate dielectrics of TFTs. The different gate insulators were used depending on the channel layer because the conduction band offset (for n-type TFT) between the gate dielectric and channel should be a lager than 1 eV (Figure 2.5). By this condition, HfO_2 and Al_2O_3 were used for polycrystalline/epitaxial SnO_2 TFTs and for $ZnGa_2O_4$ TFTs, respectively.

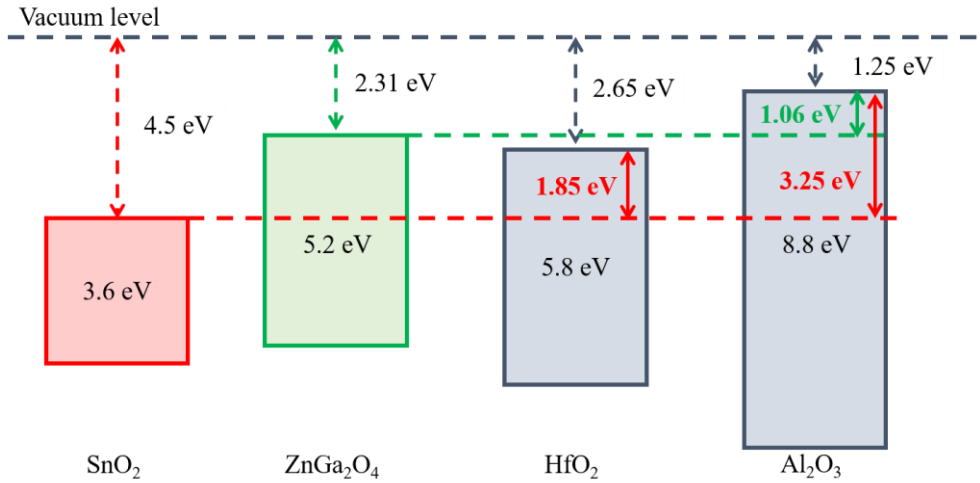

Figure 2.5. Band offset of SnO_2 [25], $ZnGa_2O_4$ [10, 30], HfO_2, and Al_2O_3 [31].

HfO_2 deposition proceeded at 250 ℃ with TEMAHf (Tetrakis(ethyl-methylamido)hafnium, 4[$(C_2H_5)(CH_3)N$]Hf) and H_2O as precursors. The growth rate of HfO_2 under the conditions was 1 Å/cycle. Meanwhile, Al_2O_3 was used as a gate dielectric which was deposited at 220 ℃ with TMA (trimethylaluminum, $Al_2(CH_3)_6$) and H_2O sources. With the conditions, Al_2O_3 was grown by 1 Å per cycle.

During the ALD process, hydrogens coming from precursors remained within the channel layer and gate insulator. This exerted influences on the channel layer to doped by hydrogen and having the low channel resistance. The residual hydrogens have affecting to not only the channel but also the gate insulator to having high leakage current. To prevent this, the post-ALD annealing process was carried out at 400 ℃ for an hour in flowing oxygen.

Chapter 3. Thin film transistors based on polycrystalline SnO_{2-x} and epitaxial SnO_{2-x}

3.1 SnO_2 as transparent conductive oxide (TCO) / transparent oxide semiconductor (TOS)

Optical transparency is incompatible with electrical conductivity because transparency requires wide bandgap over 3.1 eV. Large bandgap is difficult for doping and generating carriers. In this sense, transparent conductive oxide (TCO) and transparent oxide semiconductor (TOS) satisfying optical transparency and electrical conductivity at the same time are especially important to optoelectronics and display applications. The known TCO/TOS are In_2O_3:Sn (ITO), ZnO, In_2O_3-Ga_2O_3-$(ZnO)_m$ (IGZO), and SnO_2.

For flat panel display including liquid crystal display (LCD), hydrogenated amorphous silicon (a-Si:H) has been used. However, the low mobility below 1 cm^2/Vs and a small bandgap of a-Si:H devices limit the device performances. To overcome the limitations and replace a-Si:H, the needs for the low temperature deposited TCO/TOS with high mobility about 10 cm^2/Vs have been raised. For satisfying the demand, IGZO emerged as amorphous TCO with high mobility. Through single-crystalline $InGaO_3(ZnO)_5$ TFT with amorphous HfO_2 gate insulator on yttria-stabilized zirconia (YSZ) substrate (Figure 3.1), the high mobility of IGZO TFT was proved ($\mu_{FE} \sim 80$ cm^2/Vs) [32]. From the subsequent report [33], amorphous IGZO (a-IGZO) TFT on a flexible substrate exhibited saturation field

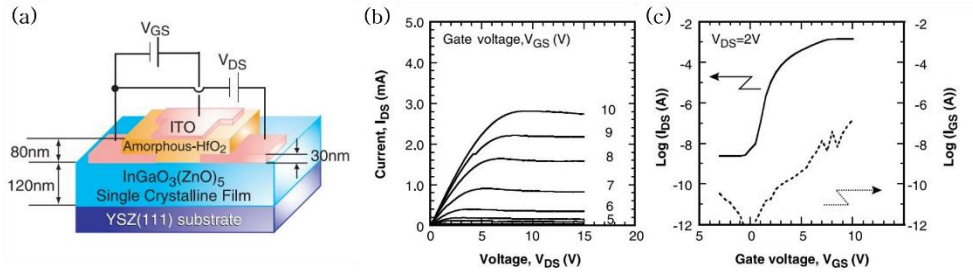

Figure 3.1. Crystalline $InGaO_3(ZnO)_5$ TFT. (a) Illustration of the TFT structure. (b) Output characteristics. (c) Transfer characteristics. Field effect mobility of ~ 80 cm^2/Vs and the on-off ratio of ~ 10^6 are obtained [32].

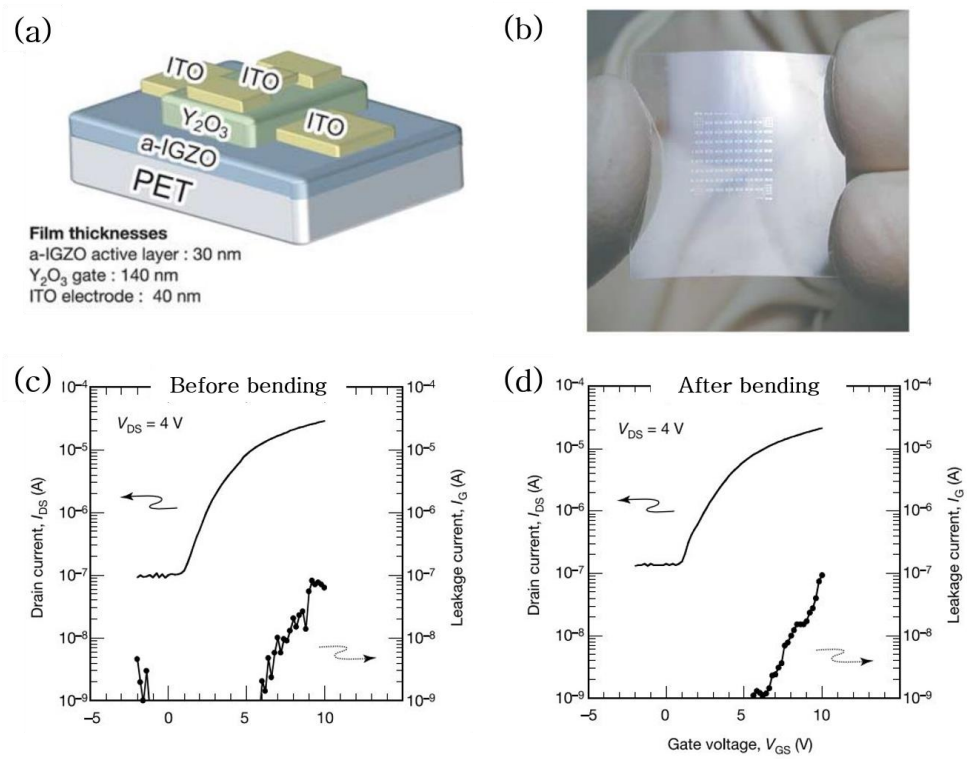

Figure 3.2. Amorphous IGZO TFT on a flexible substrate. (a) Illustration of the TFT structure. (b) A photograph of the flexible TFT sheet. (c) Transfer characteristic before bending (saturation mobility ~ 8.3 cm^2/Vs). (d) Transfer characteristic after bending (saturation mobility ~ 7 cm^2/Vs). [33]

effect mobility of ~ 8.3 cm^2/Vs (before bending) and ~ 7 cm^2/Vs (after bending) (Figure 3.2). Amorphous IGZO possessing high mobility and optical transparency is currently used for display applications including LCDs. Due to its 20 ~ 50 times higher mobility than a-Si:H, IGZO has the advantages of high resolution, low power consumption, and low noise in display devices. However, IGZO has a drawback of using expensive indium, the investigation of other TCO/TOS showing high mobility on glass or flexible substrates without indium is required.

To investigate high mobility TFT based on TCO/TOS with glass/flexible substrates, the nature abundant Sn is used. Owing to the dual valency of Sn^{2+} and Sn^{4+}, tin oxide has two stable states. SnO is a p-type oxide state of Sn^{2+} with 2.5 ~3 eV bandgap. Figure 3.3 (a) shows the tetragonal SnO crystal structure of the corner shared SnO_4 square pyramid. For SnO, SnO_{1+x} appears to be a p-type semiconductor with extra oxygens [27, 34]. Using p-type SnO, p-type TFT and complementary metal-oxide-semiconductor (CMOS) with n-type IGZO were demonstrated [35, 36].

The other phase of tin oxide is SnO_2 which is an n-type oxide state of Sn^{4+}. The crystal structure of SnO_2 is rutile structure based on the corner and edge shared SnO_6 octahedra as shown in Figure 3.3 (b) [27, 37]. SnO_2 has a wide bandgap of 3.6 eV and high optical transparency up to 97% transmittance of thin films in the visible range. Besides optical transparency, it is known that SnO_2 exhibits chemical and thermal oxygen stabilities [28, 38-40]. Figure 3.4 shows the oxygen thermal stability of epitaxial SnO_2 thin film on r-Al_2O_3. When changing the background atmosphere from argon, oxygen, and air at 500 ℃, the conductance change and stabilization of epitaxial SnO_2 thin film takes several hours which means that the oxygen diffusion process is slow and the oxygen vacancies in SnO_2 once formed are quite stable. Moreover, the conductance change of SnO_2 in the air is only about 0.5 %. This demonstrates the exceptional thermal oxygen stability of epitaxial SnO_2 thin films. [28]

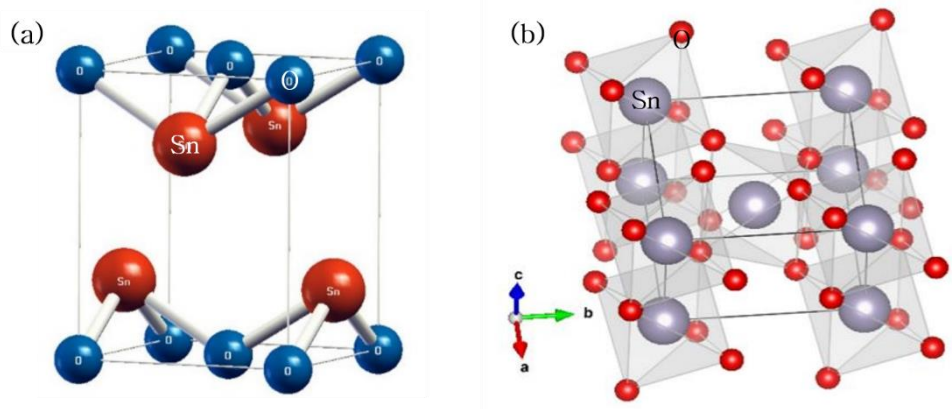

Figure 3.3. Crystal structures of (a) SnO [30] and (b) SnO_2 [37].

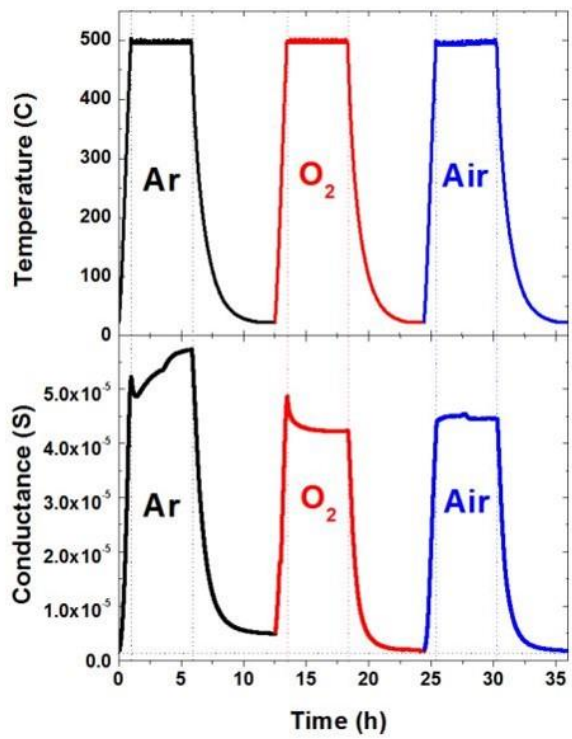

Figure 3.4. Conductance changes of the 100 nm thickness epitaxial SnO_2 thin film on r-Al_2O_3 during a thermal annealing cycle under argon, oxygen, and air atmosphere [28].

Despite the coexistence difficulty of optical transparency and high conductivity, SnO_2 is known to be able to have a wide range of carrier density, 10^{16} ~ 10^{21} cm^{-3}, and its resistivity range of 10^{-4} ~ 10^{6} Ω·cm which is low enough to be used as a TCO (10^{-3} ~ 10^{9} Ω·cm for most semiconductors) [41]. Due to the exceptional low resistivity and high carrier density (> 10^{20} cm^{-3}) along with high optical transparency, SnO_2 has been intensively studied as a TCO. Examples are Sb-doped SnO_2 [42], F-doped SnO_2 [43], and Ta-doped SnO_2 [44].

From the SnO_2 transparency, electrical properties, and stabilities, SnO_2 is not only a good TCO but also one of the promising TOS candidates. Especially, SnO_{2-x} occurs to be an n-type semiconductor with oxygen vacancies and is attractive as a TOS. In this case, the oxygen vacancies act as shallow donor levels and can be controlled with an oxygen atmosphere during or after the growth [41, 45]. For distinguishing the insulating SnO_2 from the intentional oxygen vacancy doped conducting SnO_2, SnO_{2-x} notation is used for the conducting SnO_2. Comparing with a TCO aspect of SnO_2, SnO_2 studies as TOS with good electrical properties, such as high mobility, are not many as TCO studies. A SnO_{2-x} single crystal was reported to exhibit mobility value as high 240 cm^2/Vs with a carrier density of 1.3×10^{17} cm^{-3} [46]. An epitaxial SnO_{2-x} thin film on r-Al_2O_3 with mobility of 106 cm^2/Vs and carrier density of 3.8×10^{18} cm^{-3} was demonstrated by pulsed laser ablation [28]. There have been several reports on thin film transistors based on polycrystalline SnO_2 with diverse gate dielectrics as shown in Table 3.1 and 3.2: Sb-doped SnO_2/SiO_2 [47], SnO_2/Al_2O_3 [48], SnO_2/ZrO_2 [49], SnO_2/HfO_2 [50], SnO_2/SiO_2-Al_2O_3-HfO_2 [51], and SnO_2/HfO_2 [27]. All these reports used a bottom gate structure and reported high mobility values between 96 cm^2/Vs and 279 cm^2/Vs except for our previous report [27], which used a top gate structure with its mobility value about 20 cm^2/Vs. As showing the previous studies, SnO_2 exhibits high mobility over 100 cm^2/Vs in TOS regime (carrier density ~ 10^{18} cm^{-3}), for single crystal [46], epitaxial thin film [28], and the previously reported bottom gate geometry TFTs based on polycrystalline SnO_2 [47, 49-51]. To comprehensively understand and evaluate the possibility to display and optoelectronics devices, demonstration of top and bottom gate geometry TFTs based

on polycrystalline and epitaxial SnO_2 are required.

Channel/Substrate [Reference no.]	**Deposition method**	**Gate dielectric**	**Mobility [cm^2/Vs]**
Sb-doped SnO_2/Glass [47]	RF sputtering	SiO_2	158
SnO_{2-x}/Glass [48]	Sol-gel	Al_2O_3	96
SnO_{2-x}/Glass [49]	Sol-gel	ZrO_2	103
SnO_{2-x}/Si wafer [50]	Physical vapor deposition	HfO_2	147
SnO_{2-x}/Si wafer [51]	Physical vapor deposition	$SiO_2/Al_2O_3/HfO_2$	238

Table 3.1. Bottom gate geometry thin film transistors based on polycrystalline SnO_2 with diverse gate dielectrics.

Channel/Substrate [Reference no.]	**Deposition method**	**Gate dielectric**	**Mobility [cm^2/Vs]**
SnO_{2-x}/Glass [27]	Reactive sputtering	HfO_2	20

Table 3.2. Top gate geometry thin film transistors based on polycrystalline SnO_2 with diverse gate dielectrics.

3.2 Thin film transistors based on polycrystalline SnO_{2-x}

To evaluate the possibility to display/optoelectronics devices of SnO_2, the top and bottom gate geometries TFTs of polycrystalline SnO_2 were fabricated on glass under 400 ℃ fabrication temperature. The oxygen vacancies were used as the charge carriers in the channel layer. Before the TFT fabrication, the SnO_2 structural and electrical properties were confirmed as thin films by X-ray diffraction (XRD) and transmission electron microscopy (TEM) as shown in Figure 3.5. The theta-2theta diffraction pattern of 300 nm thick polycrystalline SnO_{2-x} film on a glass shows that the peaks are corresponding to SnO_2 (110), (101), and (211). In addition to XRD data, the TEM image also proved the polycrystalline SnO_{2-x}.

Using the Van der Pauw Hall measurement, the electric transport properties of 20nm thick SnO_{2-x} film on glass were measured as follows: the Hall mobility 6.6 cm^2/Vs and n-type carrier density 6.7×10^{18} cm^{-3} for O_2:Ar = 7:3 during the reactive sputtering. From the XRD analysis and the Hall measurement, it was confirmed that the SnO_{2-x} films are the SnO_2 phase.

Based on the thin film properties, the TFTs were fabricated in the top and the bottom gate geometries as shown in Figure 3.6. Referring to the previous SnO_2 TFT report [27], HfO_2 and ITO were used to the gate insulator and source, drain, and gate electrodes of SnO_2 TFT, respectively. All layers of SnO_{2-x} channel, HfO_2 gate oxide, and ITO electrodes including glass substrates are optically transparent, fabricating transparent TFTs. The TFTs with staggered structure as shown in Figure 3.6 (a) and (b) exhibited better TFT performances than the coplanar structure TFT. For the patterned TFT fabrication, Si and stainless steel stencil masks were used.

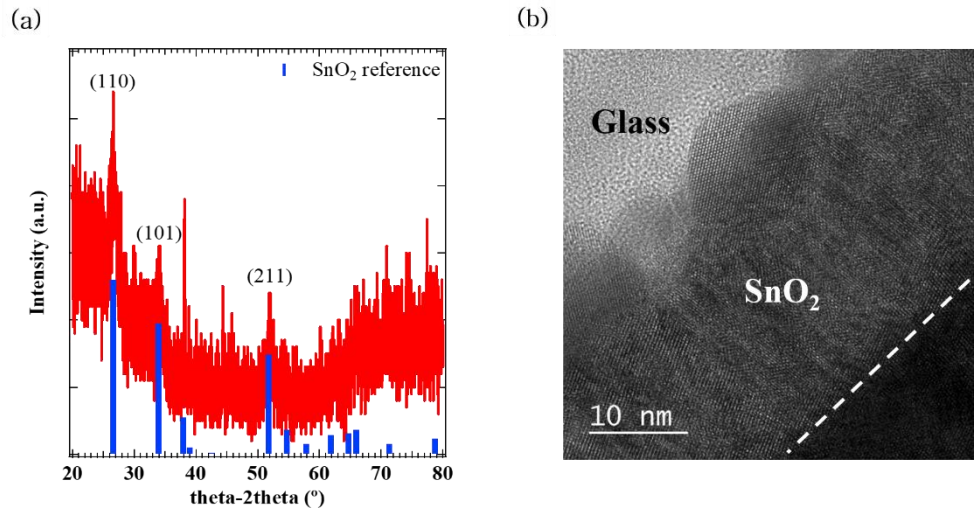

Figure 3.5. Polycrystalline SnO_{2-x} crystal structure after the post-deposition process. (a) XRD image of an annealed 300 nm thick polycrystalline SnO_{2-x} film shows the SnO_2 phase. (b) TEM image shows that SnO_{2-x} is polycrystalline.

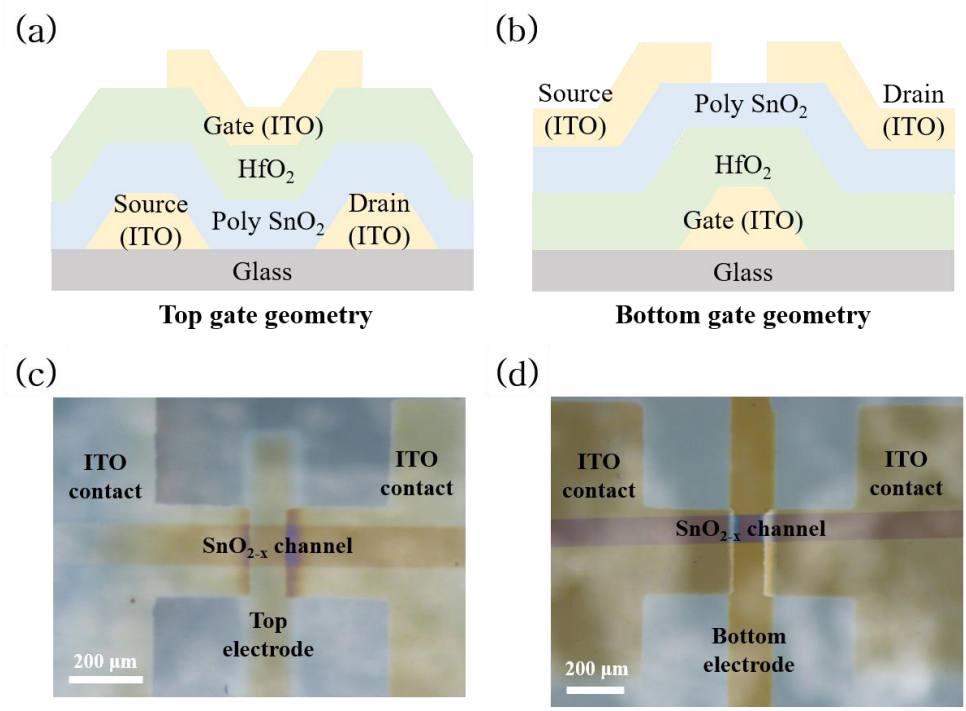

Figure 3.6. Cross-sectional schematics (a) of top gate geometry TFT and (b) of bottom gate geometry TFT. Top view optical microscope images (c) of top gate geometry TFT and (d) of bottom gate geometry TFT.

Before the SnO_{2-x} TFTs fabrication, the dielectric properties of HfO_2 were checked through MIM (metal-insulator-metal) capacitors with ITO electrodes. The capacitance-frequency (C-F) and current-voltage (I-V) characteristics were measured (Figure 3.7). After the post-ALD annealing process, the dielectric constant of HfO_2 was calculated to be 24 from the measured capacitance per unit area (2.7×10^{-7} F/cm^2), and the breakdown field was over 4 MV/cm. This dielectric constant value is consistent with other previous works [31, 52].

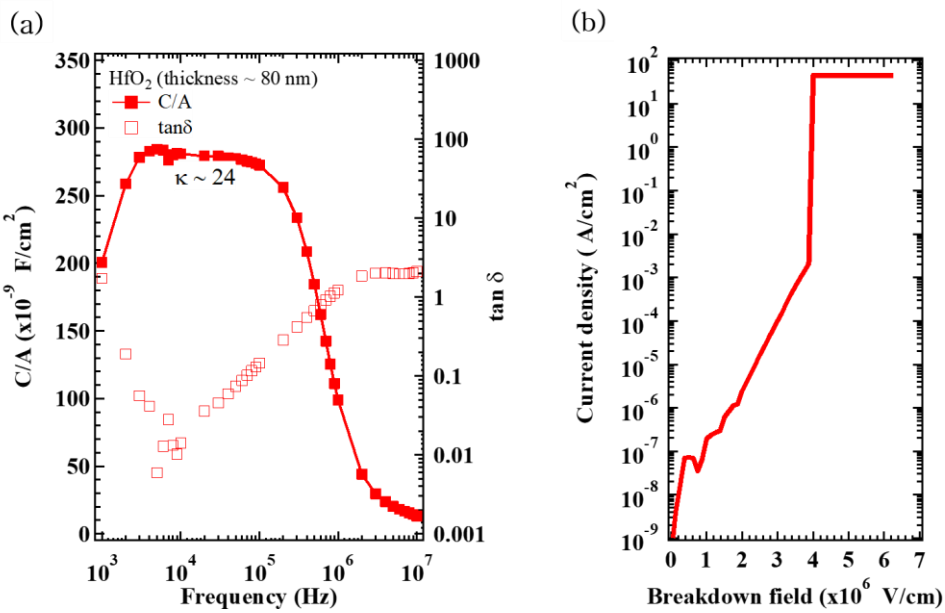

Figure 3.7. HfO_2 capacitor with ITO electrodes. (a) Capacitance-Frequency measurement of HfO_2. The calculated dielectric constant from capacitance per unit area was 24 which is consistent with the previously reported values. (b) Breakdown field from the current-voltage measurement. The breakdown field was 4 MV/cm.

3.2.1 Dependence on channel conditions

To optimize the TFT channel conditions, the TFTs were fabricated under the various SnO_{2-x} deposition conditions with top gate geometry. Figure 3.8 (a) exhibits the oxygen partial pressure dependence of TFTs. Fixing total pressure as 2 mTorr, the oxygen partial pressure was changed as O_2:Ar = 5:5, 7:3, and 9:1. The channel thickness, width, and length were 10 nm, 95 μm, and 110 μm. The I_{DS} values were measured in the linear region (V_{DS} = 1 V). As an increasing oxygen ratio, the charge carriers decrease because the oxygen vacancies act as charge carriers of SnO_{2-x}. With an increase in the oxygen partial pressure from 50 % (Figure 3.8 (a) green) to 70% (Figure 3.8 (a) yellow), TFTs showed the improved TFTs characteristics of higher mobility. With further increase in oxygen partial pressure to 90 % (Figure 3.8 (a) blue), TFTs performances were significantly degenerated due to carriers decrease. At O_2:Ar = 7:3 (Figure 3.8 (a) yellow) showed the highest field effect mobility over 60 cm^2/Vs.

To check dependence on the channel thickness, the 10 nm thick and 20 nm thick SnO_{2-x} TFTs were fabricated with the channel dimension of width 180 μm and length 110 μm. The total pressure and oxygen partial pressure during the SnO_2 deposition were 2 mTorr and O_2:Ar =7:3. Transfer characteristics (Figure 3.8 (b)) were measured in the linear region of V_{DS} = 1V. The 20 nm thick SnO_{2-x} TFT (Figure 3.8 (b) red) showed higher mobility than 10 nm thick SnO_{2-x} TFT (Figure 3.8 (b) yellow). Based on these results, the channel conditions of 20 nm channel thickness and O_2:Ar = 7:3 were used for polycrystalline SnO_{2-x} TFTs. The Hall measurement results of the 20 nm thick polycrystalline SnO_{2-x} thin film deposited at the O_2:Ar = 7:3 conditions were Hall mobility 6.6 cm^2/Vs and the n-type carrier density 6.7×10^{18} cm^{-3}.

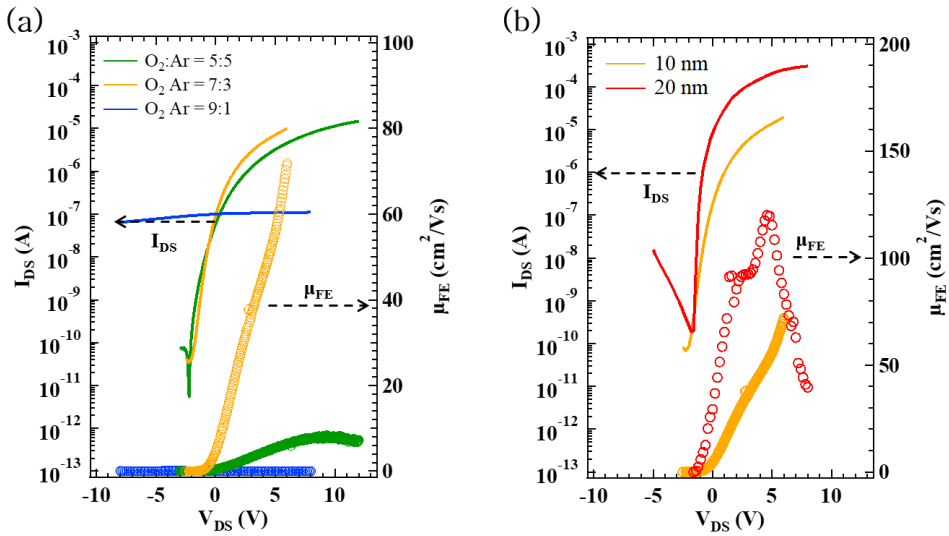

Figure 3.8. Top gate geometry TFTs depending on the channel conditions. The total pressure during the SnO_{2-x} deposition was fixed as 2 mTorr. (a) The oxygen partial pressure dependence. (b) The channel thickness dependence with the O_2:Ar = 7:3.

3.2.2 Thin film transistors characteristics

The top and the bottom gate geometries TFTs were fabricated with the polycrystalline channel conditions of thickness 20 nm and O_2:Ar = 7:3. Figure 3.9 and Figure 3.10 show the top and the bottom gate geometries TFT characteristics, respectively. The output characteristics (Figure 3.9 (a) and Figure 3.10 (a)) were measured the source-drain current by increasing source-drain voltage at each gate-source voltage. The applied V_{GS} varied from 3 V to -2 V in 1 V steps. The output characteristics (Figure 3.9 (b) and Figure 3.10 (b)) confirm that both types of polycrystalline SnO_{2-x} TFTs operate in an n-type depletion mode. The transfer characteristics were also measured at V_{DS} 1 V which is a linear region.

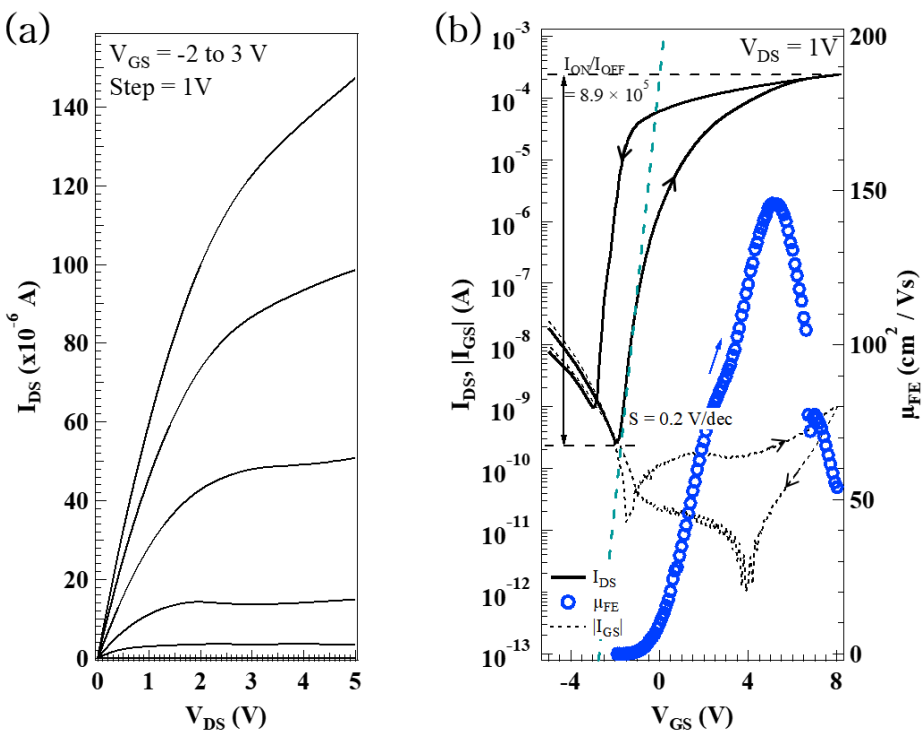

Figure 3.9. Top gate TFT based on polycrystalline SnO_{2-x}. (a) Output characteristics (I_{DS}-V_{DS}). (b) Transfer characteristics (I_{DS}-V_{GS} at V_{DS} = 1 V, linear region).

The channel length and width were 100 μm and 100 ~ 130 μm, respectively. The maximum μ_{FE} of the top and the bottom gate were 145.7 cm^2/Vs and 160.0 cm^2/Vs, respectively, in the linear region. For top gate geometry TFT, the I_{ON}/I_{OFF} value was 8.9×10^5 and the subthreshold swing (S) value was 0.2 V/dec. Bottom gate geometry TFT exhibited the I_{ON}/I_{OFF} value of 3.1×10^4 and the S-value of 0.7 V/dec. Both SnO_{2-x} TFTs exhibited much higher mobility when the carriers are accumulated by field effect than that of the thin films, probably due to the fewer oxygen vacancies in the TFT channel layer. It also implies that the SnO_{2-x} channel layer was well modulated by HfO_2 without the large influence from defects that are formed in the TFT structure.

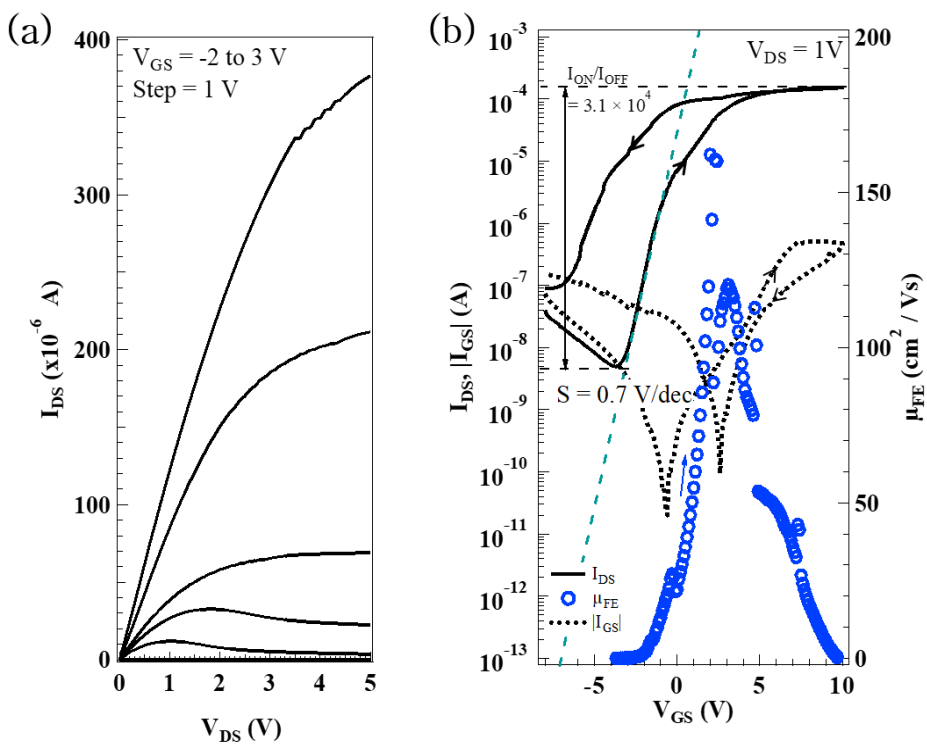

Figure 3.10. Bottom gate TFT based on polycrystalline SnO_{2-x}. (a) Output characteristics (I_{DS}-V_{DS}). (b) Transfer characteristics (I_{DS}-V_{GS} at V_{DS} = 1 V, linear region).

When comparing the output and transfer curves, the top gated TFT showed more ideal characteristics, such as clearer pinch-off in the output characteristics and lower subthreshold swing and leakage current (I_{GS}) in the transfer characteristics. These differences between the top and the bottom gate TFTs could be thought of as two possible origins. One comes from the exposure of the SnO_{2-x} channel layer to the ambient conditions in the bottom gate geometry. The other is related to the gate oxide layer. During the fabrication process, the HfO_2 gate dielectric goes through more diverse environments in the case of the bottom gate geometry, which may cause relatively high leakage current, leading to less ideal characteristics.

Figure 3.11 shows the aging effects in polycrystalline SnO_{2-x} TFTs. For two months, the devices were kept in ambient conditions. The top gate TFT in Figure 3.11 (a) seems nearly not affected by aging; the field effect mobility and the I_{ON}/I_{OFF} ratio were slightly increased and the subthreshold swing remained nearly the same. However, in the case of the bottom gate TFT in Figure 3.11 (b), the on-state current and mobility values have decreased in 2 months, showing a larger aging effect than the top gate TFTs. Since the SnO_{2-x} channel layer was exposed, various molecules might be more easily absorbed in the channel, possibly causing the on-state conductance (I_{ON}) and the mobility decrease [47, 53, 54]. The polycrystalline top gate TFT characteristics endured the aging process much better because the HfO_2 gate dielectric plays an additional role of passivation [55].

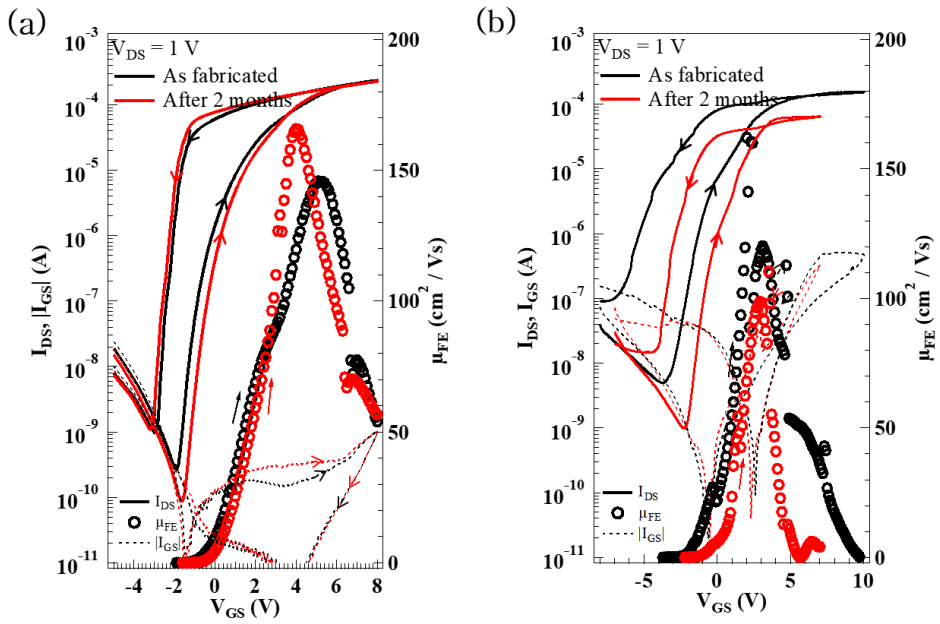

Figure 3.11. Aging effects. (a) Top gate TFT transfer curves: measurement right after fabrication (black) and measurement in 2 months (red). (b) Bottom gate TFT transfer curves: measurement right after fabrication (black) and measurement in 2 months (red).

3.2.3 Non-ideal behaviors and possible origins

Even though the high mobility, the polycrystalline SnO_{2-x} TFTs exhibited the non-ideal behaviors in their output and transfer characteristics; a large hysteresis was observed along with large voltage dependence. Both types of polycrystalline SnO_{2-x} TFTs showed non-ideality in output characteristics. As shown in Figure 3.12, the polycrystalline TFTs exhibited not the current saturation but the current decrease after the pinch-off in low V_{GS}, as indicated by arrows. These cannot be explained by the negative differential resistance caused by self-heating in other AlGaN/GaN field effect transistor (FET) and polycrystalline Si FET studies [56, 57]. The polycrystalline SnO_{2-x} TFTs showed the current decrease only in the low V_{GS} whereas the self-heating should become more severe as the current increases due to the increasing V_{GS}.

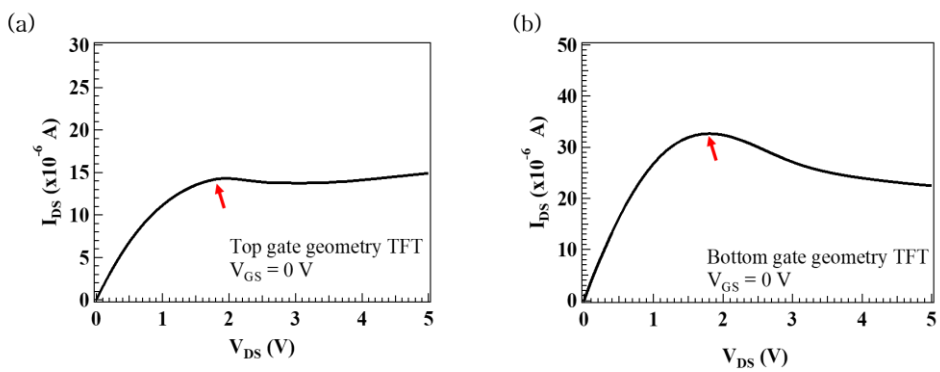

Figure 3.12. Non-ideal output characteristics in V_{GS} = 0 V (a) for the top gate geometry TFT and (b) for the bottom gate geometry TFT.

The count-clockwise hysteresis in transfer characteristics, Figure 3.9 (b) and Figure 3.10 (b), is in contrast to the field effect transistors based on a La-doped $BaSnO_3$ channel with the same HfO_2 gate oxide showing a clockwise hysteresis in transfer curve [52]. Clockwise hysteresis (for the n-type device) is known to be caused by trap states near the interface between the channel layer and the gate oxide [58]. These

trap states reduce the effective electric field by V_{GS}, causing clockwise hysteresis. On the other hand, the count-clockwise hysteresis usually occurs because of the dielectric property or defects inside the gate oxide which try to maintain the electric field even when the V_{GS} is reduced. There are three possible explanations for count-clockwise hysteresis: (1) ferroelectricity of the dielectric, (2) mobile ion in the dielectric, and (3) charge injection into the dielectric [58-60]. The first explanation could be excluded because the polarization in HfO_2 is reported to occur usually in a cubic, tetragonal, or orthorhombic phases [61, 62]. The HfO_2 monoclinic phase which is not showing the polarization is the most common and stable. The polarization phases of cubic, tetragonal, and orthorhombic are formed when HfO_2 is doped with other materials [61-63] or in particular conditions [64, 65]. The second possibility is also ruled out since we performed the same post-ALD annealing process for hydrogen elimination for both the polycrystalline SnO_{2-x} and La-doped $BaSnO_3$ TFTs [52]. Charge injection and trapping accompany an increase in leakage current as increasing V_{GS} due to tunneling process assisted by defects [58, 59]. However, our TFTs exhibited very low leakage current (I_{GS}) when compared with I_{DS}. Thus, the third explanation is also a remote possibility for the count-clockwise hysteresis in the transfer characteristics.

The polycrystalline TFTs showed the voltage (V_{DS}) dependent behaviors. Figure 3.13 exhibits the V_{DS} dependence and aging effects, simultaneously. For direct comparing of the aging effect and V_{DS} dependence within one device, the device was measured right after fabrication and after passing 5 months. After applying the saturation voltage V_{DS} = 5 V (Figure 3.13 green line), the on-state current significantly decreased and the hysteresis direction switched from the count-clockwise to the clockwise direction. In Figure 3.13, the black line, the red dotted line, and the blue dotted line represent the on-state current from the as-fabricated state, after 5 months, and after applying the saturation V_{DS}, respectively. As the current decrease, the field effect mobility decreased from 145.7 cm^2/Vs to 72.8 cm^2/Vs (after 5 months) and to 45.6 cm^2/Vs (after applying the saturation V_{DS}).

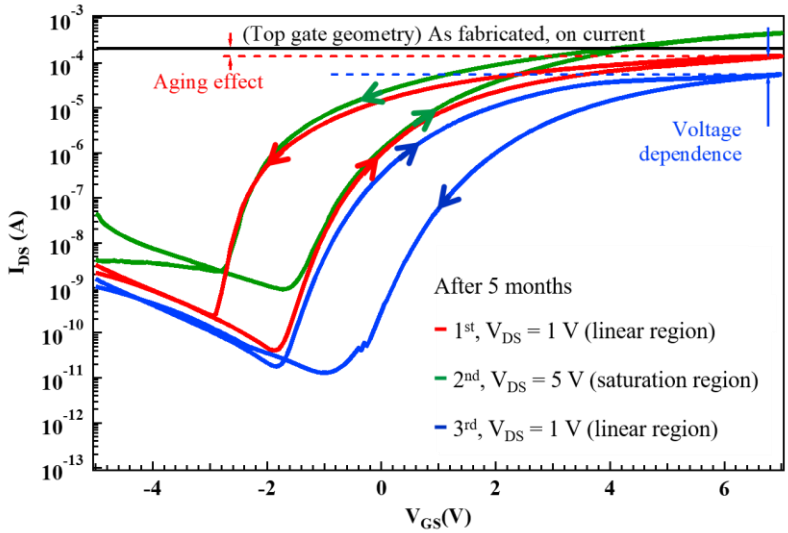

Figure 3.13. Voltage (V_{DS}) dependence in the polycrystalline SnO_{2-x} TFT: the top gate TFT transfer curve.

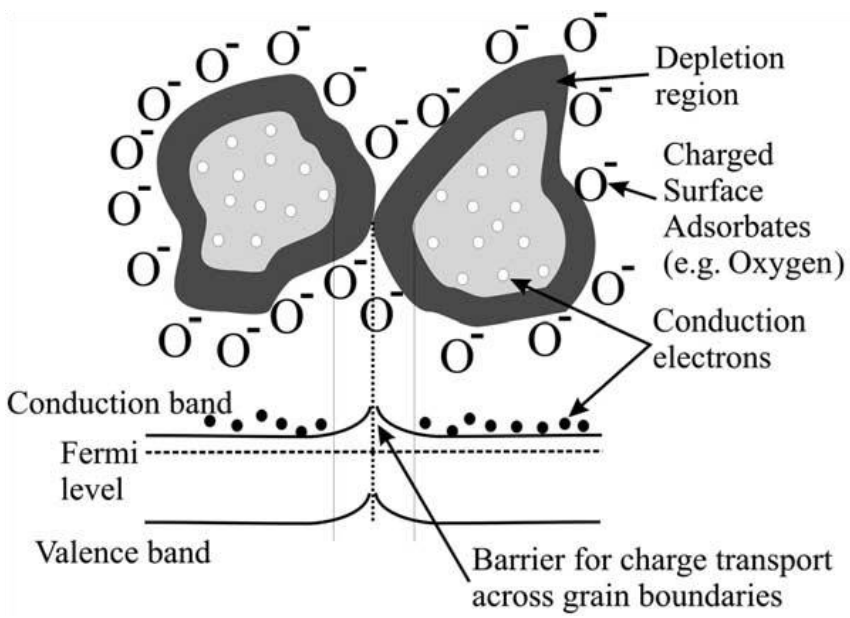

Figure 3.14. Illustration of double Schottky barrier formation at the polycrystalline SnO_2 grain boundary [45, 66, 67].

SnO_2 has been used for applications such as catalysis and solid-state gas sensor, other than TOS. These applications employ the surface and interface properties of SnO_2 which is caused by chemical adsorption of oxygen and other molecules, not by the lattice oxygen concentration. An adsorbed molecule at the surface makes electrons transfer between SnO_2 and the adsorbed molecule. This has a net charge at the surface and leads to the electric field. The electric field results in band bending. For example, O^{2-}, a negative charge makes the band bend upward and reduce charge carrier concentration. This leads to the formation of the depletion region at the grain surface. For polycrystalline SnO_2, this mechanism occurs at every grain boundary and forms a double Schottky barrier between grains as shown in Figure 3.14 [45, 67]. The grain size, the charge trap density, and the carrier density, which vary depending on the deposition conditions, seem to determine the barrier height. Such barriers are known to be related to the voltage dependence and non-ohmic behavior of the SnO_2 due to charge trapping in or near the grain boundaries. The barrier height and current flow can be controlled by applying bias. The non-ohmic behavior is known to depend on SnO_2 itself, not on the electrode material [45, 66-69]. The hysteresis direction switching after applying high V_{DS} shown in Figure 3.13 is also considered as that the current paths through the grain boundaries are sensitive to the current flowing history. When comparing Figure 3.11, Figure 3.12, and Figure 3.13, the current values (I_{DS}) seem inconsistent at V_{DS} = 1 V and V_{GS} = 0 V. The I_{DS} in Figure 3.12 is larger than the sweep up (V_{GS} varies from minus to plus bias) current in Figure 3.11 and a little smaller than the sweep down (V_{GS} varies from plus to minus bias) current. It is because of the residual effects of the charge traps at the grain boundaries. Due to the HfO_2 layer which works as the gate oxide and a passivation layer [55], the top gate structure polycrystalline TFT seems not much affected by the gas environment (Figure 3.11). However, it shows a large current decrease by voltage, indicating that the charge trapping and untrapping in grain boundaries are modifying the barrier height.

Using such a process to modify the barrier height in the current path, the SnO_2 for gas sensor changes the resistance in the gas environment. These phenomena exist

not only in polycrystalline SnO_2 but also have been reported in polycrystalline ZnO TFTs for gas sensing or varistor applications [66, 69]. To understand and control such surface-sensitive behavior of the polycrystalline SnO_2 is a complicated and difficult task because the polycrystalline SnO_2 is composed of many grains of several orientations such as (110), (101), and (211). To experimentally confirm that the grain boundary issues result in the non-ideal behaviors of polycrystalline SnO_{2-x} TFT, the TFT investigations of the epitaxial SnO_{2-x} or polycrystalline SnO_{2-x} having large grain size enough to ignore the depletion layer are required.

3.3 Thin film transistors based on epitaxial SnO_{2-x}

To confirm the grain boundary related issues of polycrystalline SnO_{2-x}, epitaxial SnO_{2-x} was used to fabricated TFT. Based on the previous study on epitaxial SnO_{2-x} films, the epitaxial SnO_{2-x} TFTs were fabricated. The epitaxial SnO_2 was grown by PLD at 800 ℃ on r-Al_2O_3. Figure 3.15 shows the theta-2theta diffraction patter of SnO_2 grown on r-Al_2O_3 by PLD. Only (101) and (202) peaks of the SnO_2 are observed, which are consistent with the previous report [28]. The specific crystal structural and electric properties of epitaxial SnO_2 thin films were reported in the study [28].

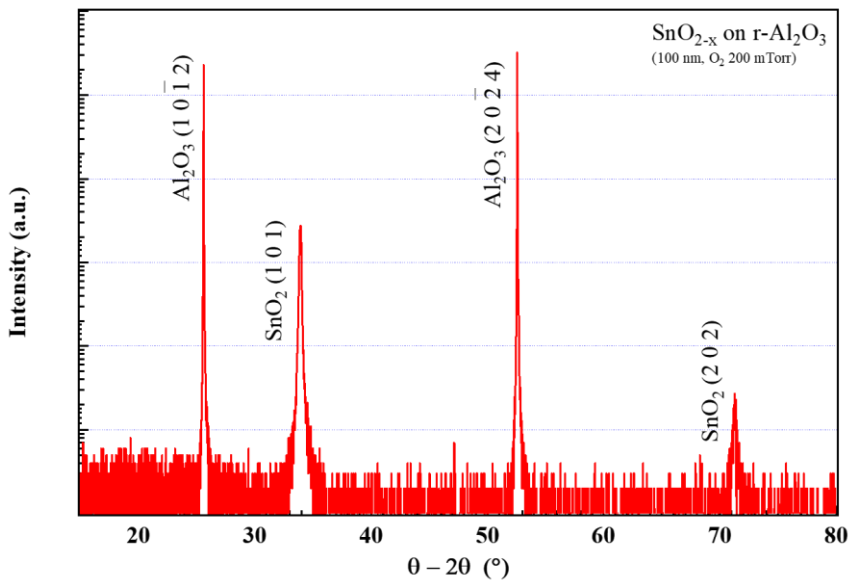

Figure 3.15. XRD data of epitaxial SnO_2 film on r-Al_2O_3.

To reduce the threading dislocations and the anti-phase boundaries effects on the channel layer, the 100 nm thick insulating SnO_2 buffer layer was deposited in 200 mTorr oxygen pressure. For creating n-type carriers in SnO_{2-x} film coming from oxygen vacancies, the 20 nm thick of epitaxial SnO_{2-x} was deposited in 50 mTorr oxygen pressure on the buffer layer. The same conditions were used for the ITO electrodes and the HfO_2 gate oxide as those for the polycrystalline SnO_{2-x} TFTs case. Figure 3.16 shows the epitaxial SnO_{2-x} TFT structure. Since the existence of the buffer layer, there was no bottom layer geometry TFT based on epitaxial SnO_{2-x}.

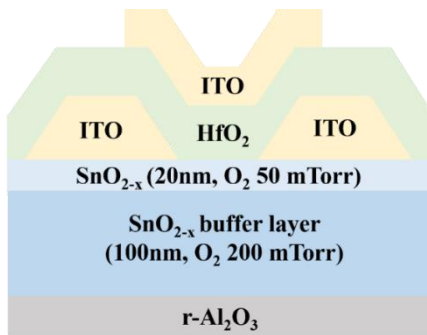

Figure 3.16. Cross-sectional schematic of epitaxial SnO_{2-x} TFT.

3.3.1 Thin film transistors characteristics

The epitaxial devices showed ideal saturation behavior of an n-type depletion mode in its output characteristics, shown in Figure 3.17 (a). As shown in Figure 3.17 (b), the field effect mobility, I_{ON}/I_{OFF}, and the subthreshold swing (S) values were 20.5 cm^2/Vs, 2.3×10^6, and 0.6 V/dec, respectively. The hysteresis curve in the transfer characteristics was found to be clockwise, a usual behavior coming from the defects near the interface with the HfO_2 gate dielectric. Although the field effect mobility was not as high as that of the polycrystalline SnO_{2-x} TFT, there was no decrease in I_{ON} current or change in the hysteresis direction after applying various V_{DS}, although a shift of the threshold voltage has been observed (Figure 3.18).

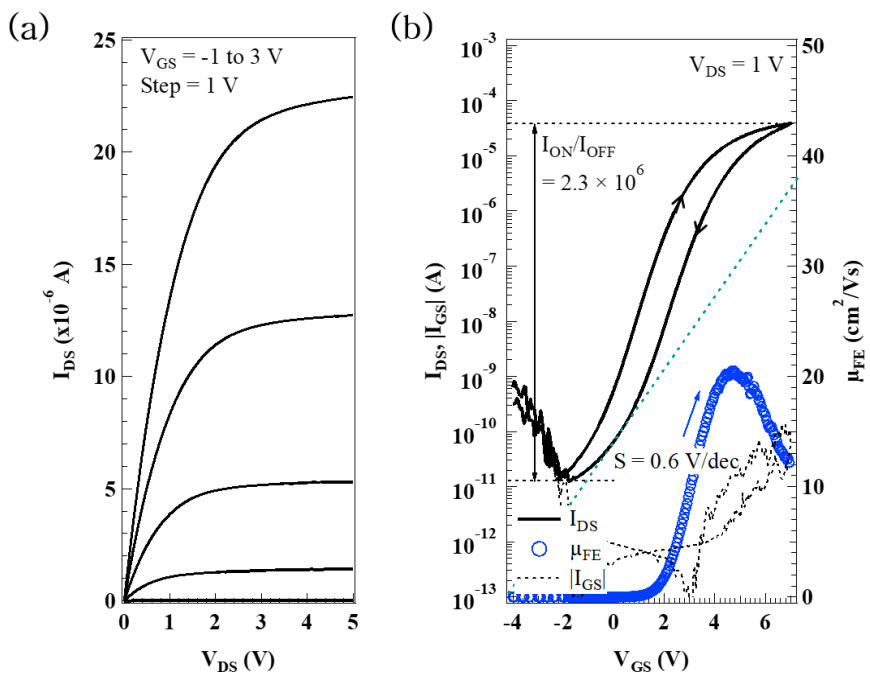

Figure 3.17. Epitaxial SnO_{2-x} TFT. (a) Output characteristics (I_{DS}-V_{DS}). (b) Transfer characteristics (I_{DS}-V_{GS} at V_{DS} = 1 V, linear region).

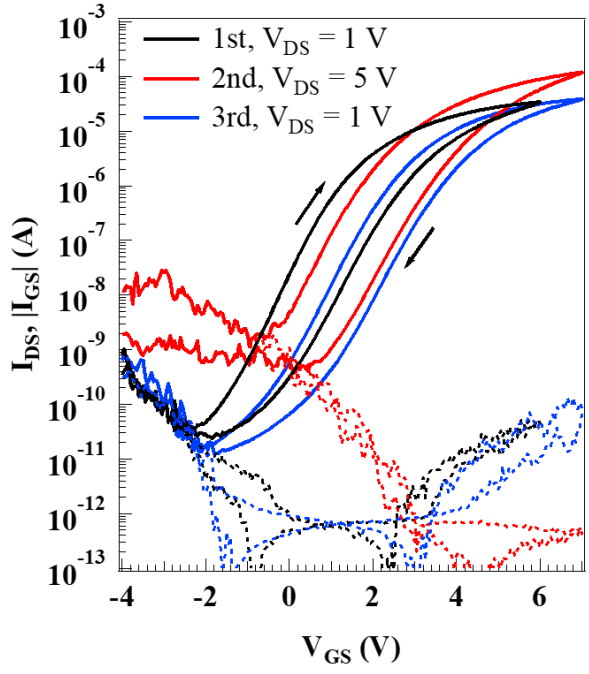

Figure 3.18. V_{DS} dependence measurement of epitaxial SnO_{2-x} TFT.

3.3.2 Grain boundaries of polycrystalline SnO_{2-x} and threading dislocations/antiphase boundaries of epitaxial SnO_{2-x}

From the TFT performances comparing between the polycrystalline SnO_{2-x} TFTs and the epitaxial SnO_{2-x} TFTs, the grain boundary related issues of the polycrystalline SnO_2 were experimentally confirmed. However, the field effect mobility of epitaxial SnO_{2-x} TFTs was not high as that of polycrystalline SnO_{2-x} TFT. Following the previous studies [28, 70], the existence of high density threading dislocations and anti-phase boundaries in epitaxial SnO_2 could explain for the lower mobility in the epitaxial TFTs (Figure 3.19). In particular, on the r-Al_2O_3 substrates 4 SnO_2 lattice spacing plus 1 anti-phase boundary repeat in every 2.57 nm. This compensates for the large mismatch with the substrate [70]. On the other hand, the grain size in the polycrystalline SnO_2 is approximately 7 ~ 10 nm from the XRD and the TEM data. Therefore, there are more crystalline defects in the epitaxial SnO_2. Although the crystalline defects in epitaxial SnO_{2-x} do not seem to affect the stability, they seem to be the cause for the lower mobility in epitaxial SnO_{2-x}. Polycrystalline SnO_{2-x} grain boundaries seem responsible for the instability, such as hysteretic behavior and voltage dependence, but its effect on mobility seems negligible.

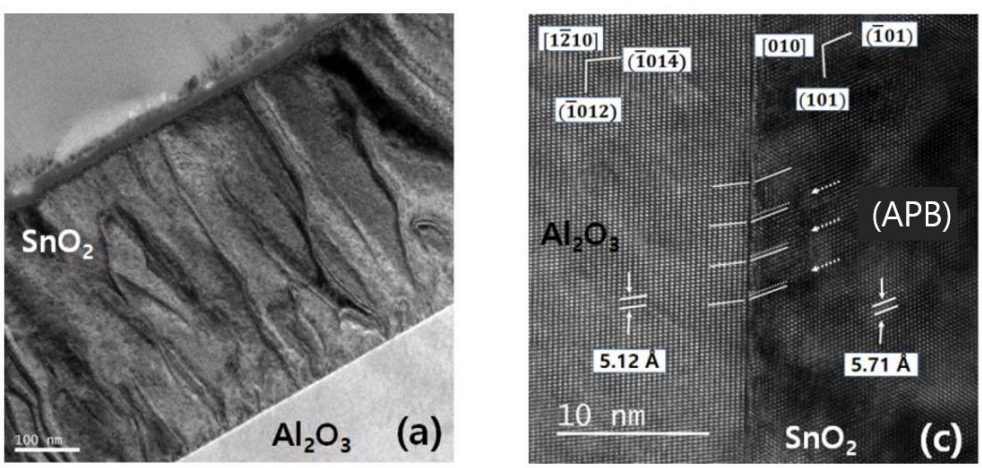

Figure 3.19. TEM images of epitaxial SnO_2 thin film on r-Al_2O_3 [28].

In summary, transparent thin film transistors of polycrystalline SnO_{2-x} and epitaxial SnO_{2-x} were demonstrated with HfO_2 gate dielectric. The polycrystalline SnO_{2-x} TFTs were fabricated in both the top and the bottom gate geometries, showing non-ideal output characteristics, count-clockwise hysteresis, and V_{DS} dependence in transfer characteristics, despite the high mobility over 100 cm^2/Vs. No such non-ideal behaviors were observed for the epitaxial SnO_{2-x} TFT, suggesting that the grain boundaries in SnO_{2-x} are the origin of such behaviors. On the other hand, if the crystalline defects in the epitaxial SnO_{2-x} are reduced, it will be possible to demonstrate epitaxial SnO_{2-x} TFTs with mobility as high as those of the polycrystalline SnO_{2-x} TFTs without the TFTs performances instability. Furthermore, the use of polycrystalline SnO_{2-x} TFTs will require a thorough understanding of grain boundaries in SnO_{2-x}.

Chapter 4. Thin film transistors based on $ZnGa_2O_4$

4.1 Ultra-wide bandgap spinel oxide $ZnGa_2O_4$

Because of its abundance in nature, the spinel (AB_2X_4, X = O, S, or Se) structure has attracted a lot of attention. Among the various spinel materials, the spinel oxides (AB_2O_4) have been investigated from several points of view such as superconductivity [71], magnetism [72-74], and multiferroicity [75]. Using these properties, spinel oxides have been studied for applications in spin-dependent or high-frequency devices. On the other hand, the transport properties of some spinel oxides have been reported to explore their potential as transparent conductive oxides (TCO), for example in Cd_2SnO_4 [76].

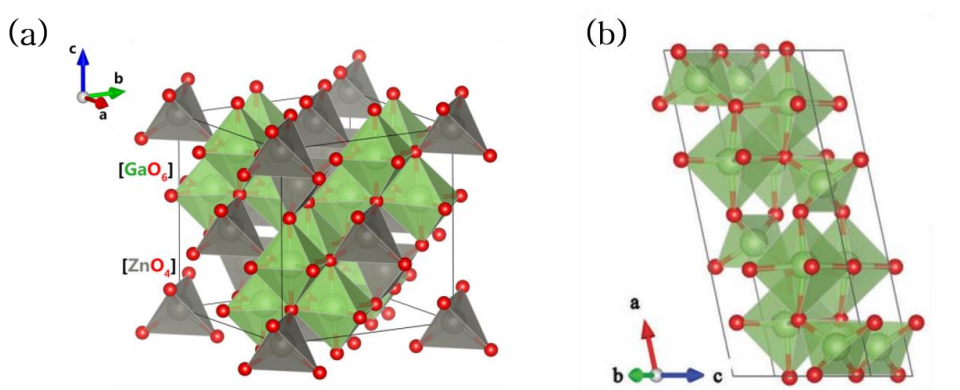

Figure 4.1. Crystal structure of (a) $ZnGa_2O_4$ (normal cubic spinel, a = b = c = 8.33 Å) [77] and (b) β-Ga_2O_3 (monoclinic) [78].

Among the ultra-wide bandgap semiconductors, monoclinic β-Ga_2O_3 (E_g = 4.8 ~ 4.9 eV) [4, 7] is being investigated widely for high power applications due to its availability as large wafers, n-type doping controllability through Si or Sn dopant (resistivity: 10^{-3} ~ 10^{12} Ω·cm, carrier density: 10^{15} ~ 10^{19} cm^{-3}), and the expected high breakdown field over 9 MV/cm [4, 13]. Despite these advantages, β-Ga_2O_3 suffers from several issues arising from anisotropic optical, thermal, structural, and mechanical properties along with polymorphs. Moreover, there have not been reported of β-Ga_2O_3 p-type doping.

$ZnGa_2O_4$ (ZGO) is spotlighted as an ultra-wide bandgap transparent semiconductor oxide with a normal spinel structure and a bandgap of 4.6 ~ 5.2 eV (Figure 4.1 (a)) [8-10]. Such large bandgap values of ZGO were measured both for single-crystal and for thin films. Bulk ZGO single-crystals and corresponding wafers for epitaxy were successfully prepared and their electrical properties were reported [8]. High electron mobility (~ 100 cm^2/Vs) at high free electron concentration (mid 10^{19} cm^{-3}) reported for bulk ZGO crystals confirms that the network of edge-shared GaO_6 possesses wide bandgap and high mobility as in the case of β-Ga_2O_3. ZGO has three major advantages over β-Ga_2O_3: (1) cubic structure, (2) high doping possibility, and (3) higher electric conductivity. The cubic spinel structure offers isotropic physical properties, no easy cleavage planes, moderate hardness, and a very stable phase. In addition to isotropic properties, ZGO has the relative free to select the substrates due to the cubic structure. ZGO is known as normal spinel which Ga^{3+} locate at the octahedral site and Zn^{2+} locates at the tetrahedral site with a low degree of inversion [79]. Besides the normal spinel structure, two cation sites offer a high doping possibility. The calculated ZGO band structure suggests that the conduction band minimum comes from Ga 4s and O 2p states and the valence band maximum results mostly from O 2p states [77]. Therefore, ideally by using a dopant that prefers to be in tetrahedral sites, one can insert the dopants away from the edge-shared GaO_6 octahedral network to minimize the disruption in the conduction band, resulting in improved mobility. Similar mobility enhancement was found in $(Ba_{1-x}La_x)SnO_3$ perovskite oxide in comparison to $Ba(Sn_{1-x}Sb_x)O_3$ [80], where the network of corner-

shared SnO_6 octahedra was minimally disrupted by the La doping instead of the Sb doping. As comparing with β-Ga_2O_3, ZGO shows higher electric conductivity (Figure 4.2). For undoped β-Ga_2O_3 and ZGO single-crystal, ZGO exhibited higher electric conductivity following as 10 ~ 500 $\Omega^{-1}\cdot cm^{-1}$ (β-Ga_2O_3 undoped single-crystal electric conductivity: 1 ~ 25 $\Omega^{-1}\cdot cm^{-1}$). As comparing doped single-crystal of β-Ga_2O_3 (by doping with Si or Sn) and ZGO (unintentionally doped), ZGO showed higher maximum mobility at high electron concentration regime ($\geq 10^{19}$ cm^{-3}) of 107 cm^2/Vs than that of β-Ga_2O_3 (50 cm^2/Vs) [8]. As shown in Figure 4.2 squares, ZGO heteroepitaxial thin films on c-Al_2O_3 exhibited much lower electric properties than the doped β-Ga_2O_3 homoepitaxial thin films on own single-crystal [10, 22, 81]. Considering that ZGO thin films are not much studied as β-Ga_2O_3 thin films, ZGO thin films are expected to show better properties through further studies.

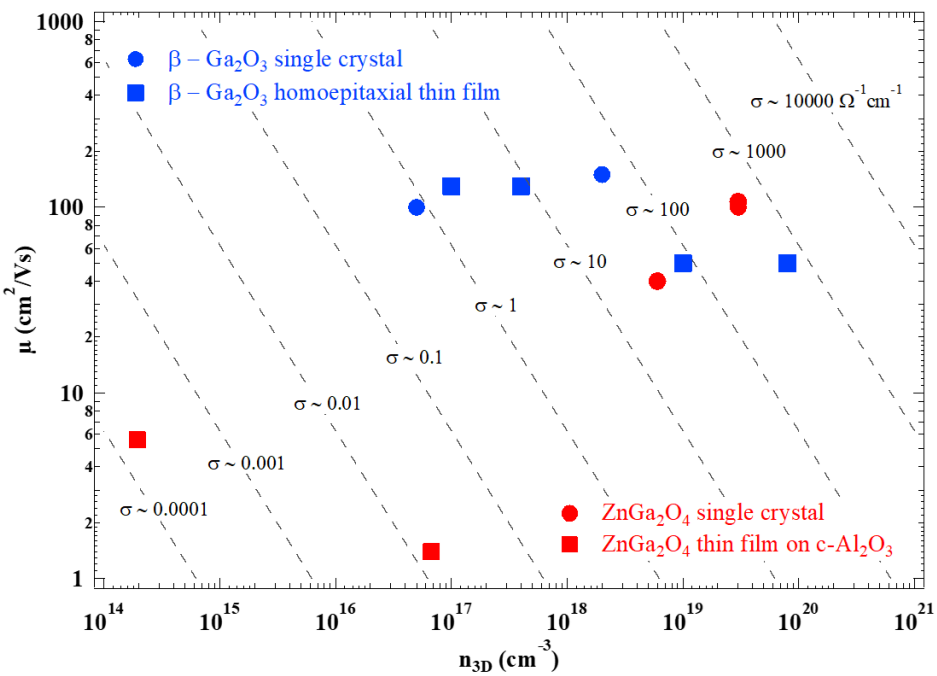

Figure 4.2. Mobility against carrier density of $ZnGa_2O_4$ and β-Ga_2O_3 [8, 10, 22, 81].

Owing to its wide bandgap and stability, ZGO has been intensively studied as an efficient phosphor of red ~ blue with several dopants [77, 82-84]. By contrast, its electrical properties as a transparent oxide semiconductor (TOS) and/or a transparent conductive oxide (TCO) were scarcely investigated in ceramic, single-crystal, or thin film form [8, 10, 24]. Only recently a few reports emerged on the field effect transistors based on epitaxial cubic ZGO which is grown on c-Al_2O_3 by metal-organic chemical vapor deposition (MOCVD) technique (Figure 4.3). Based on the reports, ZGO was grown in (111) direction on c-Al_2O_3 and ZGO field effect transistors exhibited the field effect mobility of 0.05 ~ 5.97 cm^2/Vs. [30, 85, 86]

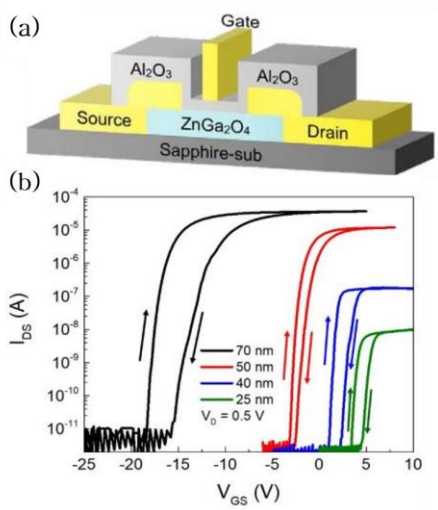

(c)

TABLE 1. Properties of different thicknesses of $ZnGa_2O_4$ TFT.

Thickness (nm)	70	50	40	25
V_{th} (V)	-17.5	-2.75	1.5	4.1
S.S (mV/dec)	330	150	160	260
μ_{FE} (cm^2/V-s)	4.2	2.6	0.3	0.054
DIBL (mV/V)	200	40	13	9
△SS (mV/dec)	410	121	110	255
V_{BK} (V)	223	308	408	401

Figure 4.3. Field effect transistors (FETs) of $ZnGa_2O_4$ (ZGO) on c-Al_2O_3. (a) Illustration of FET structure. (b) Transfer characteristics of ZGO FET depending on the ZGO channel thickness. (c) Properties of different thicknesses of ZGO FET. [30, 85, 86]

4.2 $ZnGa_2O_4$ thin films: structural and compositional properties

4.2.1 Thin films on c-Al_2O_3

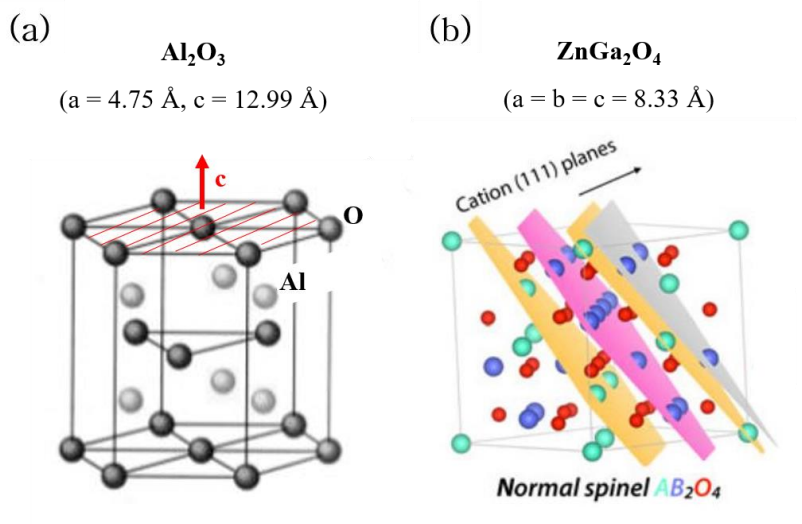

Figure 4.4. (a) Crystal structure of sapphire (Al_2O_3). Red filled surface represents c-plane. (b) Illustration of (111) plane of $ZnGa_2O_4$ [87].

Referencing the reports of $ZnGa_2O_4$ field effect transistors on c-Al_2O_3 [30, 85, 86], epitaxial ZGO growth on the c-plane sapphire substrate was first tried. As shown in Figure 4.4, it is expected that (111) oriented ZGO on c-Al_2O_3. With PLD, the sequentially alternate deposition method of Ga_2O_3 and ZnO targets was used for ZGO growth. Based on the growth ratio of each material at 750 ℃ and O_2 100 mTorr, the ideal Ga_2O_3:ZnO shot ratio was 7:12 which is based on growth rate of each material. The actual Ga_2O_3:ZnO shot ratio for ZGO without other phases of ZnO or Ga_2O_3 was 4:20~40 because of Zn volatility.

Figure 4.5 (a) shows the (111) oriented ZGO epitaxial thin film on c-Al_2O_3. Using the high resolution cross-sectional TEM (Figure 4.6), it was confirmed that (111)-oriented lattice spacing of ZGO is 4.87 Å. This is about 1 % difference with the known bulk ZGO lattice spacing of 4.808 Å. Figure 4.6 (red dotted lines) shows the ZGO grain boundaries which have a size of approximately 50 nm. Phi-scan (Figure 4.5 (b)) exhibits the ZGO peaks every 60° . From TEM and phi scan, there are two different in-plane configuration growth of ZGO on c-Al_2O_3 and seems to cause the grain boundaries with 60° difference. Along with the grain boundaries, ZGO on c-Al_2O_3 showed rough surfaces. As shown in Figure 4.7, the surface roughness was over 2 nm. Moreover, as rasing ZnO shot ratio during the deposition, the surface roughness increased and white particles which is assumed as Zn particles on the ZGO surface increased. Following the study of ferrites spinels on $MgAl_2O_4$ (100) [88], high temperature growth could result in interdiffusion of volatile components and 3 dimension island growth causing a rough surface while PLD deposition. The white particle on ZGO surface could be originated from 3 dimension island formation due to high growth temperature and volatile Zn. Therefore, lower temperature growth will make it possible to grow epitaxial robust films with a smooth surface. During the low temperature growth, insufficient kinetic energy can be compensated by decreasing oxygen pressure. [88]

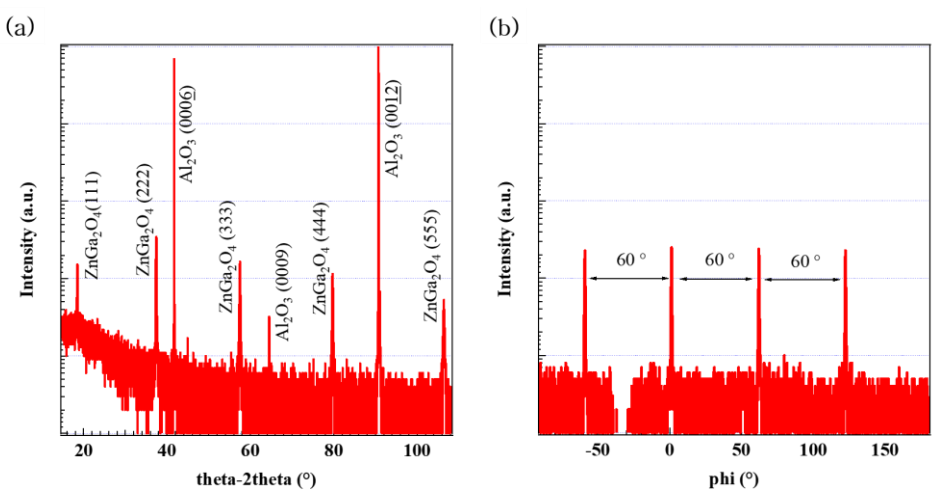

Figure 4.5. XRD data of ZGO thin films on c-Al_2O_3. (a) Theta-2theta scan. (b) Phi scan.

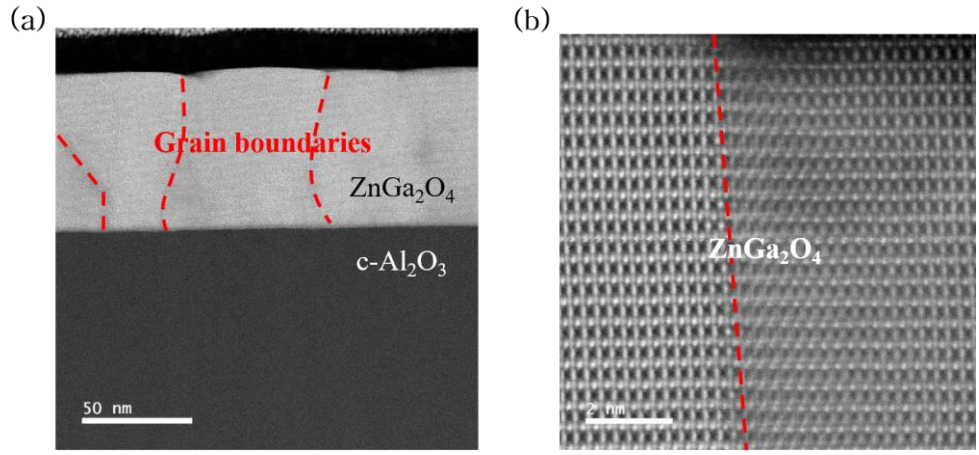

Figure 4.6. TEM images of ZGO thin films on c-Al_2O_3.

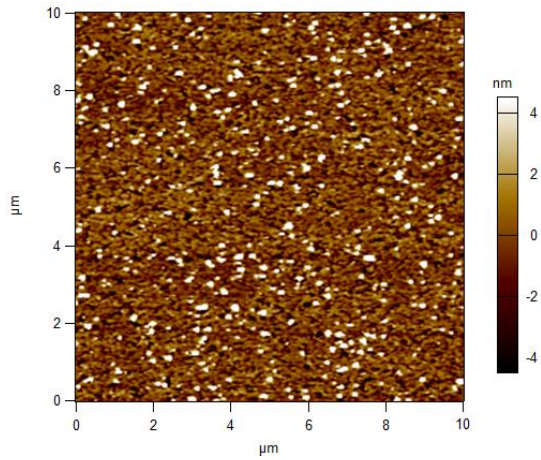

Figure 4.7. AFM images of ZGO on c-Al_2O_3. The surface roughness of ZGO was over 2 nm.

4.2.2 Thin films on $MgAl_2O_4$

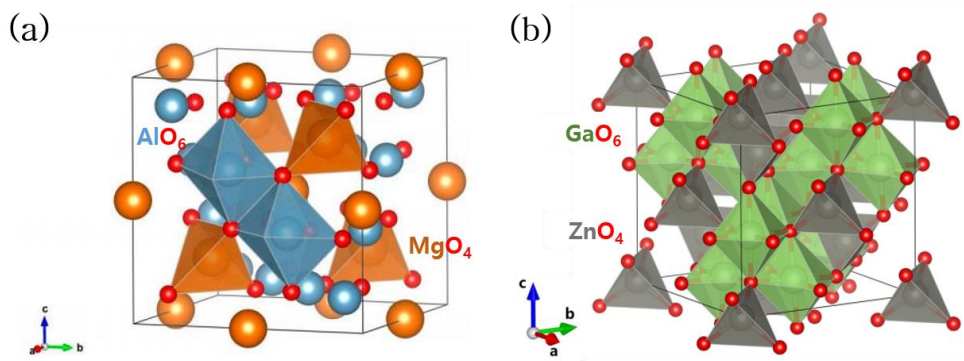

Figure 4.8. Crystal structures of (a) $MgAl_2O_4$ [89] and (b) $ZnGa_2O_4$ [77].

Since ZGO on c-Al_2O_3 exhibits the grain boundaries and rough surfaces, ZGO was grown by using $MgAl_2O_4$ (MAO) as a substrate which is a normal cubic spinel structure like ZGO (Figure 4.8). The bulk lattice constants of MAO are a = b = c = 8.08 Å. As the lattice constant of ZGO is approximately 3 % larger than that of MAO substrates, in-plane compressive strain in ZGO films was expected. For robust smooth film growth, the ZGO thin films on MAO were grown at a low temperature of 450 ℃ and at a low oxygen pressure of 10 mTorr referring to the previous ferrite spinel growth study [88].

Because of the Zn volatility at high temperature, more Zn was added by alternative depositing from each of the ZGO and ZnO ceramic targets. The control of the Zn ration was achieved by the pulse shot ratio on the ZGO and ZnO targets; ZGO:ZnO pulse shot ratio was changed from 10:0, 10:3, 10:7, eventually to 10:10. It was made sure that less than one unit cell height of ZGO was deposited during each cycle.

To check the in-plane and out-of-plane crystallinity of ZGO thin films on substrates, a reciprocal space map (RSM) was used. RSM is a series of rocking curves, representing the shape of a given Bragg reflection in a two-dimensional reciprocal space. The wave vectors Q_X and Q_Z represent directions parallel and perpendicular

to the substrate surface. Especially, RSM is useful to interpret in-plane and out-of-plane crystal defects at the same time. From RSM data showing peak displacement, peak broadening, or peak overlap, the epitaxial layer crystallinity could be interpreted. For example, the relaxation of the epitaxial layer from strain gotten from a substrate is accompanied by tilting and peak displacement from the substrate peak. Mismatch and threading dislocations in the epitaxial layer are represented as peak broadening.

Figure 4.9 shows the RSM around ZGO (226) and MAO (226) peaks depending on the ZGO:ZnO shot ratio. In Figure 4.9 (a), (b), and (c), the Q_x values of ZGO (226) peak are perfectly pinned with the substrate MAO (226) peak, which means that ZGO thin films were grown on the MAO substrate with compressive strain in a coherent epitaxial matter. However, the lattice constant of ZGO films in the growth direction was increasing as the ZnO was added. When more ZnO was added in the ZGO:ZnO = 10:10 ratio in Figure 4.9 (d), ZGO (226) peak is no longer pinned with the substrate peak and becomes broad with the relatively weak intensity. In means that, as the ZGO unit cell gets bigger by adding more ZnO, the films started to relax in the plane of the growth by creating dislocations. Based on these Q_X and Q_Z values of ZGO (226) in RSM and theta-2theta scan (Figure 4.10), the in-plane (red triangles in Figure 4.11) and out-of-plane (red squared in Figure 4.11) lattice constants of ZGO thin film in each ZGO:ZnO ratio were obtained. In-plane lattice constants are consistent with the MAO lattice constant and change imperceptibly from 8.07 Å (for 10:0) to 8.08 Å (for 10:10). On the other hand, the out-of-plane lattice constant of the ZGO films grows significantly and the unit cell volume increase accordingly (blue circles in Figure 4.11). The out-of-plane constant seems saturated at around 8.59 Å beyond the 10:7 ratio. Despite the notable expansion in the out-of-plane lattice constant, the ZGO thin film at the 10:7 ratio on MAO has still 3 % smaller unit cell volume than the known bulk ZGO (blue dashed line in Figure 4.11 ~ 578 $Å^3$) [8].

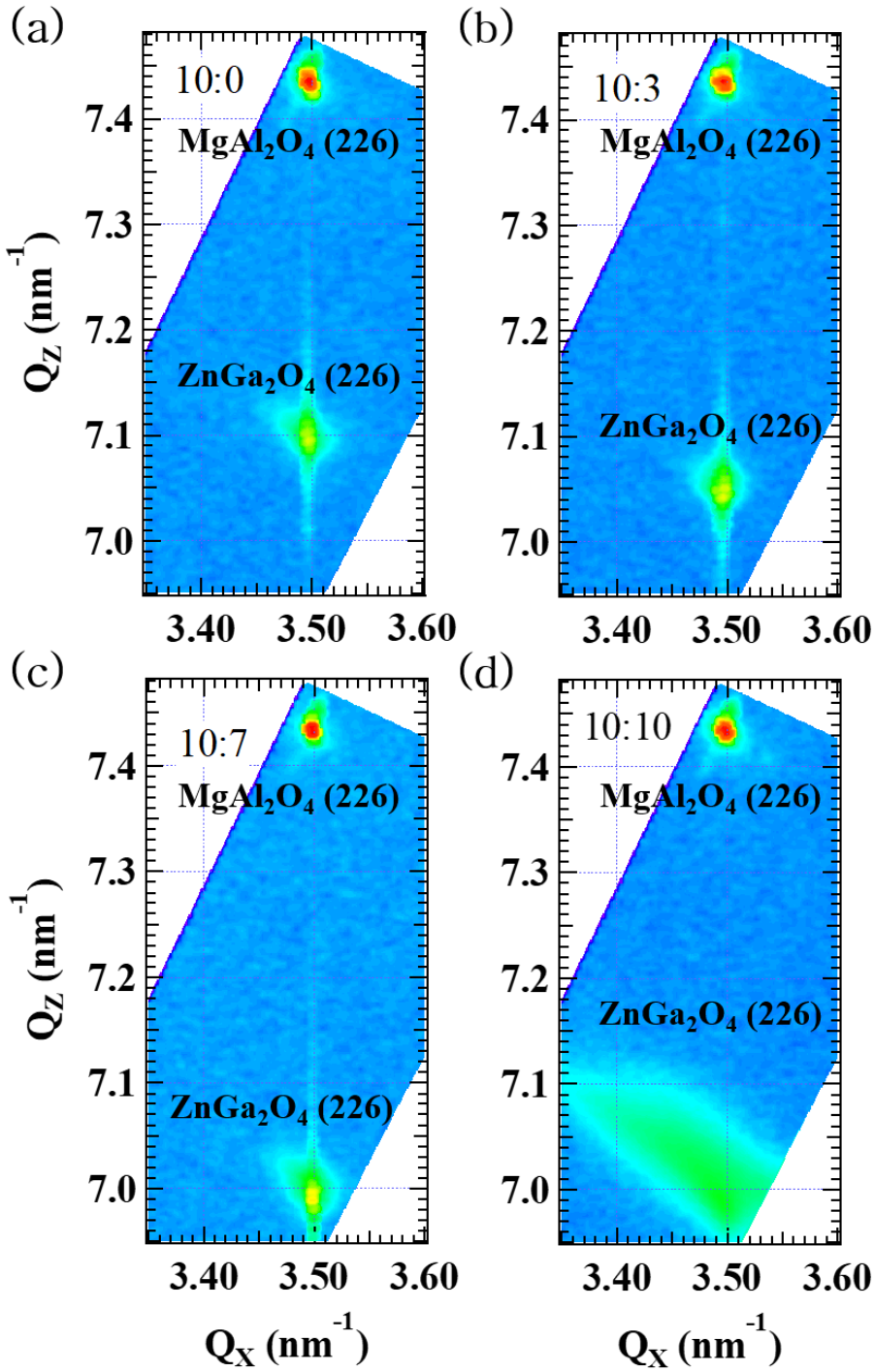

Figure 4.9. RSM of ZGO thin films on MAO (100). ZGO with (a) 10:0, (b) 10:3, (c) 10:7, and (d) 10:10.

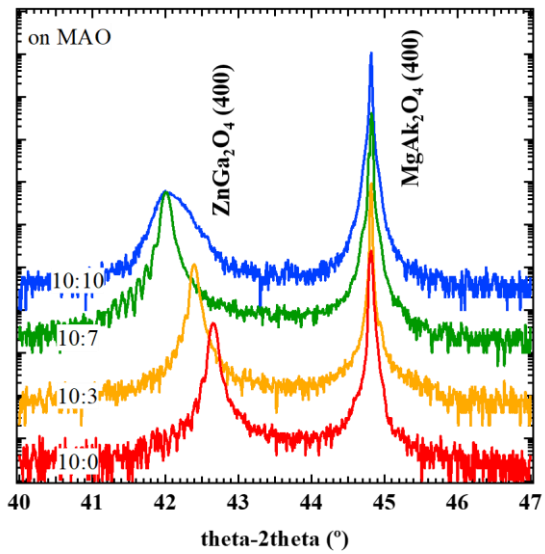

Figure 4.10. Theta-2theta scan of ZGO films on MAO substrates depending on the ZGO:ZnO shot ratio.

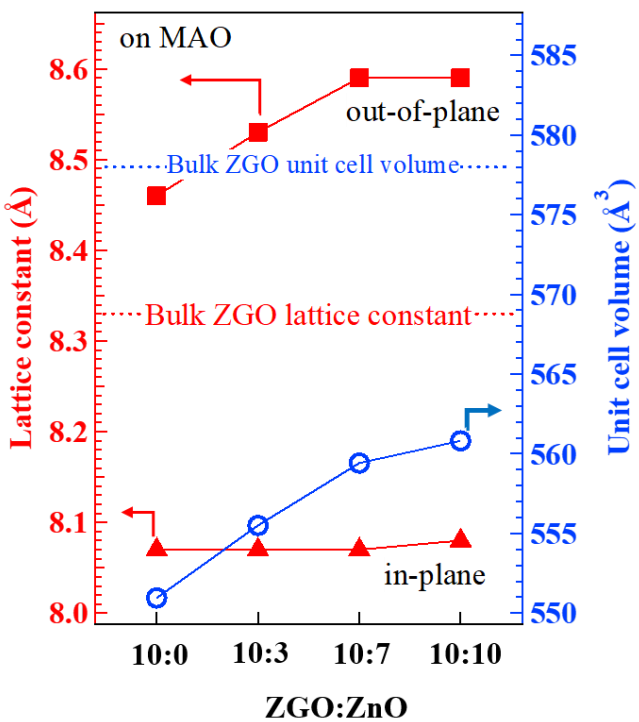

Figure 4.11. The lattice constants and unit cell volumes of ZGO on MAO (100) depending on ZGO:ZnO shot ratio.

In the RSM and theta-2theta scan (Figure 4.9 and Figure 4.10), the interference fringes at both sides of the ZGO peaks can be used to deduce the thickness of the ZGO films, which is about 100 nm, consistent with the measurement by a thickness profiler. The observed fringes also prove indirectly the presence of a smooth surface of the ZGO thin films [90]. The smooth surfaces of ZGO thin films were confirmed by AFM (Figure 4.12). Regardless of the ZGO:ZnO ratio, all the ZGO thin films on MAO showed an RMS surface roughness smaller than 330 pm.

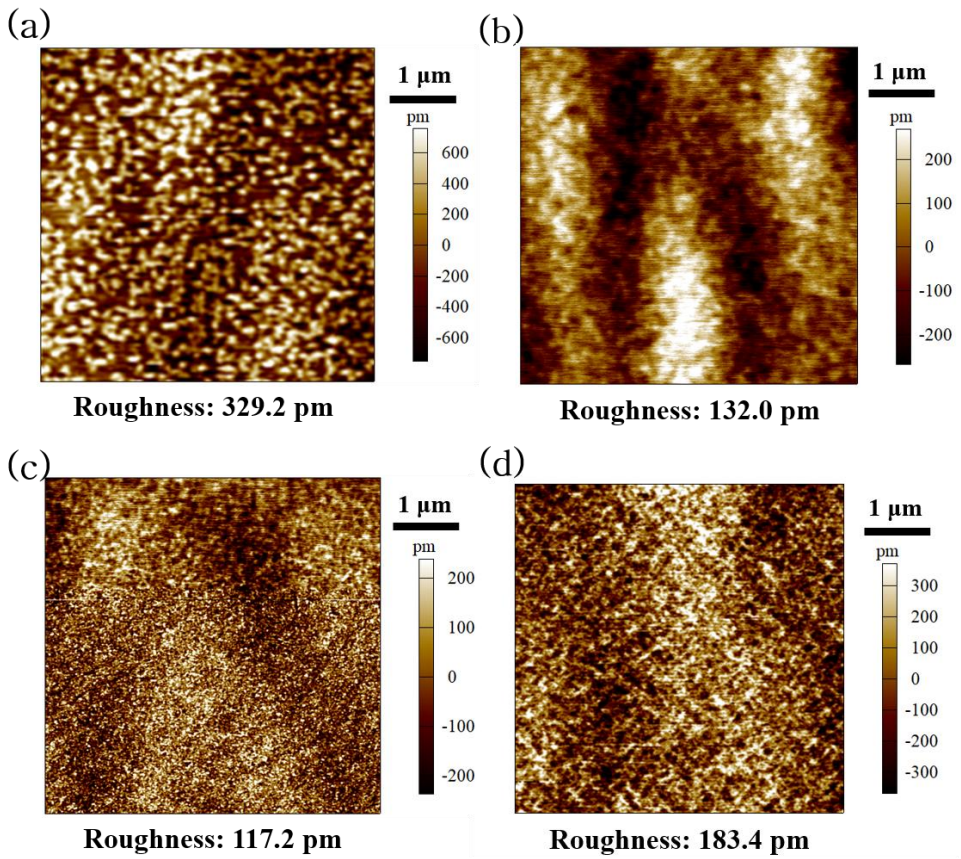

Figure 4.12. AFM images and surface roughness of ZGO thin films on MAO depending on ZGO:ZnO shot ratio of (a) 10:0, (b) 10:3, (c) 10:7, and (d) 10:10.

Besides the investigation of ZGO crystal structure depending on the ZGO:ZnO shot ratio, Zn-Ga compositional ratio in the ZGO films was measured by using EDS (energy-dispersive X-ray spectroscopy) with an SEM (scanning electron microscope). Figure 4.13 shows the cation atomic compositional ratio depending on the ZGO:ZnO shot ratio. The ratio of an insulating bulk single crystal of ZGO obtained from the meld [8] was found to be 0.48, very close to the ideal case of 0.5. For the ZGO thin films obtained on MAO substrates, the Zn/Ga ratio in ZGO increases with the increase of the ZnO shot ratio. For the ZGO:ZnO ratios 10:0 and 10:3, the Zn/Ga ratios are 0.11 and 0.25, respectively. Zn seems to be significantly deficient in these 10:0 and 10:3 ratio conditions. At the 10:7 ratio, the cation compositional ratio approaches the ideal value of 0.41. The Zn/Ga ratio of 0.51 in the 10:10 shot ratio condition is found to be slightly higher than that of the bulk ZGO single crystal and ideal value.

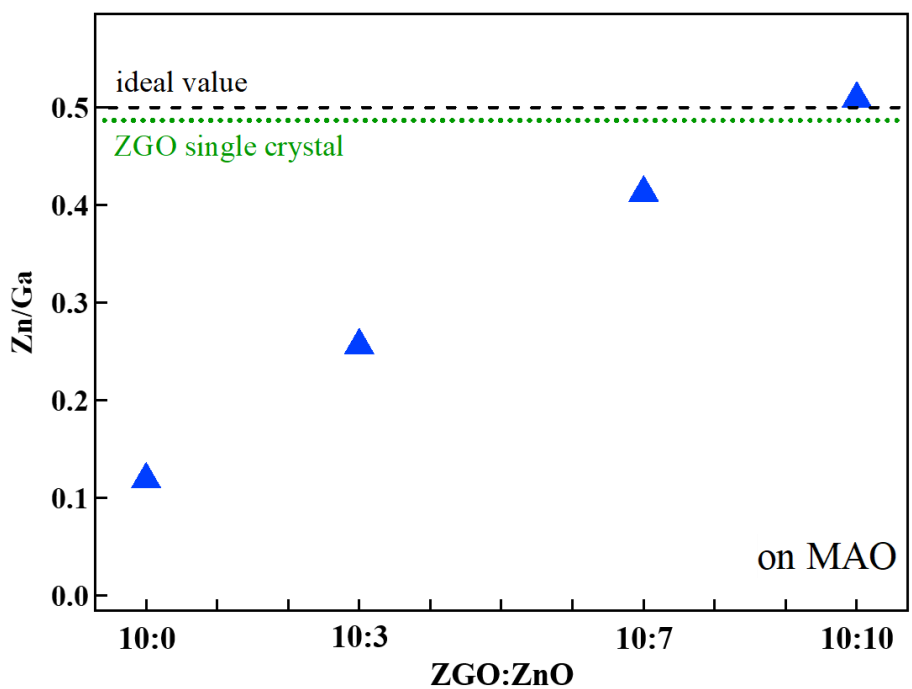

Figure 4.13. Zn-Ga compositional ratio on MAO substrate measurement by EDS with SEM.

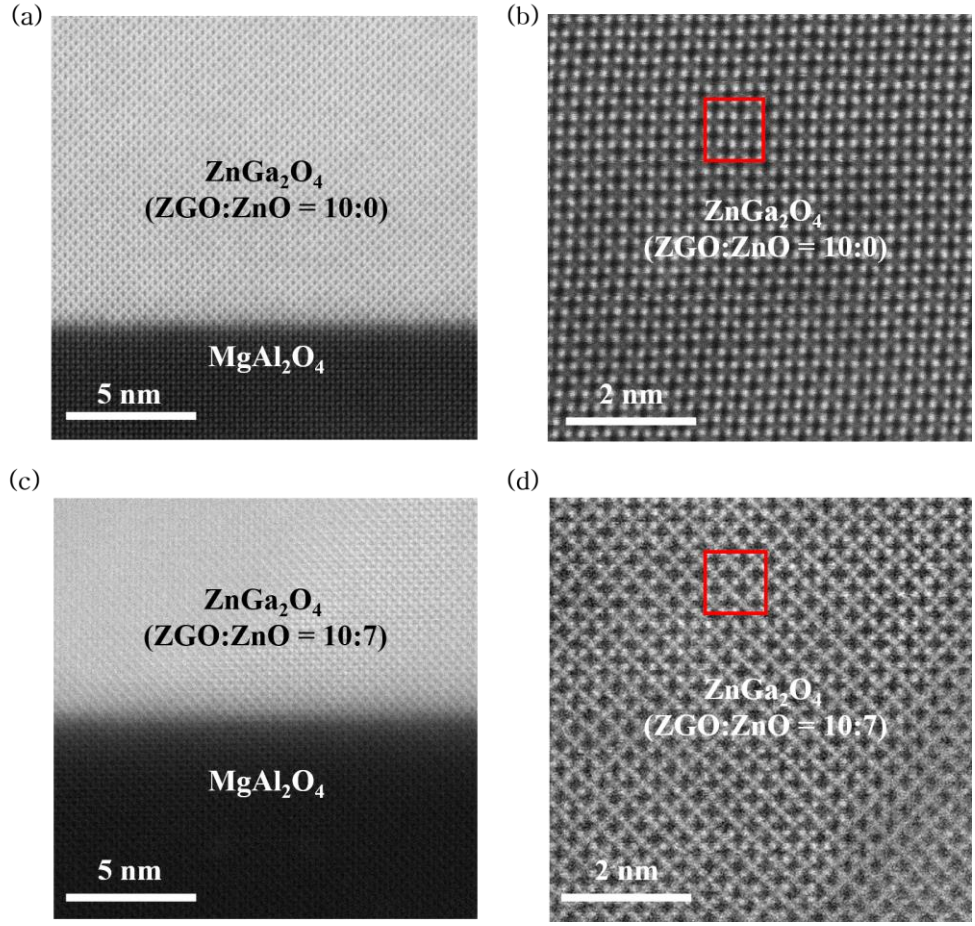

Figure 4.14. TEM images of ZGO on an MAO. (a) ZGO (ZGO:ZnO = 10:0) interface with MAO substrate. (b) ZGO (ZGO:ZnO = 10:0) away from the interface. (c) ZGO (ZGO:ZnO = 10:7) interface with MAO substrate. (d) ZGO (ZGO:ZnO = 10:7) away from the interface. Red rectangle in (b) and (d) represent ZGO unit cell.

To check the microstructure of the ZGO films on MAO, transmission electron microscopy (TEM) was used for observing cross-sections of the thin films. Figure 4.14 shows the high-resolution TEM image of the 10:0 and 10:7 ZGO films on MAO substrate. Figure 4.14 (a) and (c) clearly shows coherent epitaxial growth without misfit/threading dislocations. Figure 4.14 (b) and (d) display the TEM images of the ZGO thin films in higher resolution, where the red rectangles represent a ZGO unit cell. Despite the substantial Zn/Ga ratio difference between 10:0 and 10:7 ratio, the microstructural differences were imperceptible depending on ZGO:ZnO shot ratio.

Considering the brightest dots representing Ga and the light grey dots representing Zn, the edge-shared GaO_6 octahedra in ZGO appear to follow the edge-shared AlO_6 octahedra in the MAO substrates. Our ZGO thin films on MAO exhibited a single-crystal like crystal structure as long as we do not add too much Zn unlike the previously reported ZGO thin films on MAO which is the relaxed epitaxial growth with threading dislocation [9].

4.2.3 Thin films on MgO

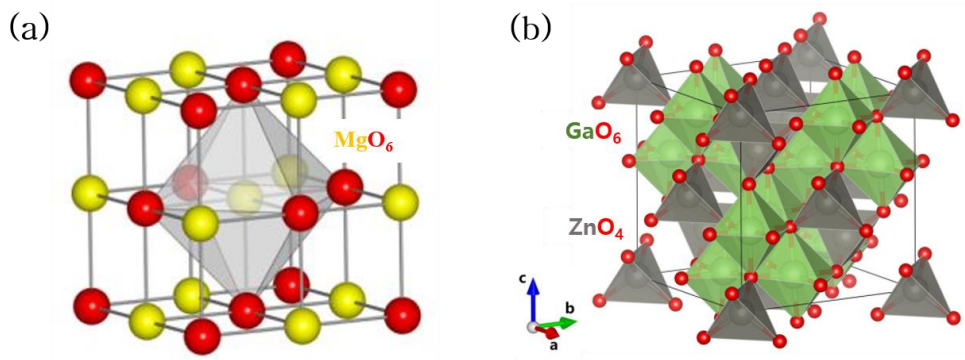

Figure 4.15. Crystal structures of (a) MgO [91] and (b) $ZnGa_2O_4$ [77].

To compare strain effects on ZGO, MgO having a cubic rocksalt structure (Figure 4.15 (a)) with the bulk lattice constant of a = b = c = 4.21 Å (8.42 Å for 2 unit cell) was also used as a substrate [92]. The ZGO lattice mismatch with the MgO substrates is about 1 % which would generate the in-plane tensile strain in the ZGO films. Figure 4.16 shows the RSM around ZGO (226) and MgO (113) peaks depending on ZGO:ZnO shot ratio of 10:0, 10:3, 10:7, and 10:10.

As shown in Figure 4.16, the ZGO peaks are located on the same Q_x values with the MgO substrate peak, suggesting coherent epitaxial growth with a tensile strain. Unlike the ZGO thin films on MAO, the ZGO thin films on MgO do not show the relaxation even at the 10:10 ratio, where the ZGO peak stays pinned with the MgO peak with excellent crystallinity. From the RSM and theta-2theta scan (Figure 4.17) of the ZGO thin films on MgO, the following in-plane lattice constants (Figure 4.18 red triangles) were obtained: 8.40 Å (for 10:0), 8.41 Å (for 10:3), 8.41 Å (for 10:7), and 8.42 Å (for 10:10). The increase in the in-plane lattice constant is almost unnoticeable, as in the case of MAO substrates. On the other hand, the out-of-plane lattice constant changed significantly (Figure 4.18 red squared): 8.05 Å (for 10:0), 8.14 Å (for 10:3), 8.22 Å (for 10:7), and 8.23 Å (for 10:10). The out-of-plane lattice constant shows a slight increase beyond the 10:7 ratio without losing crystallinity. For the 10:0 ratio, ZGO thin films on MgO have about 2 % smaller unit cell volume

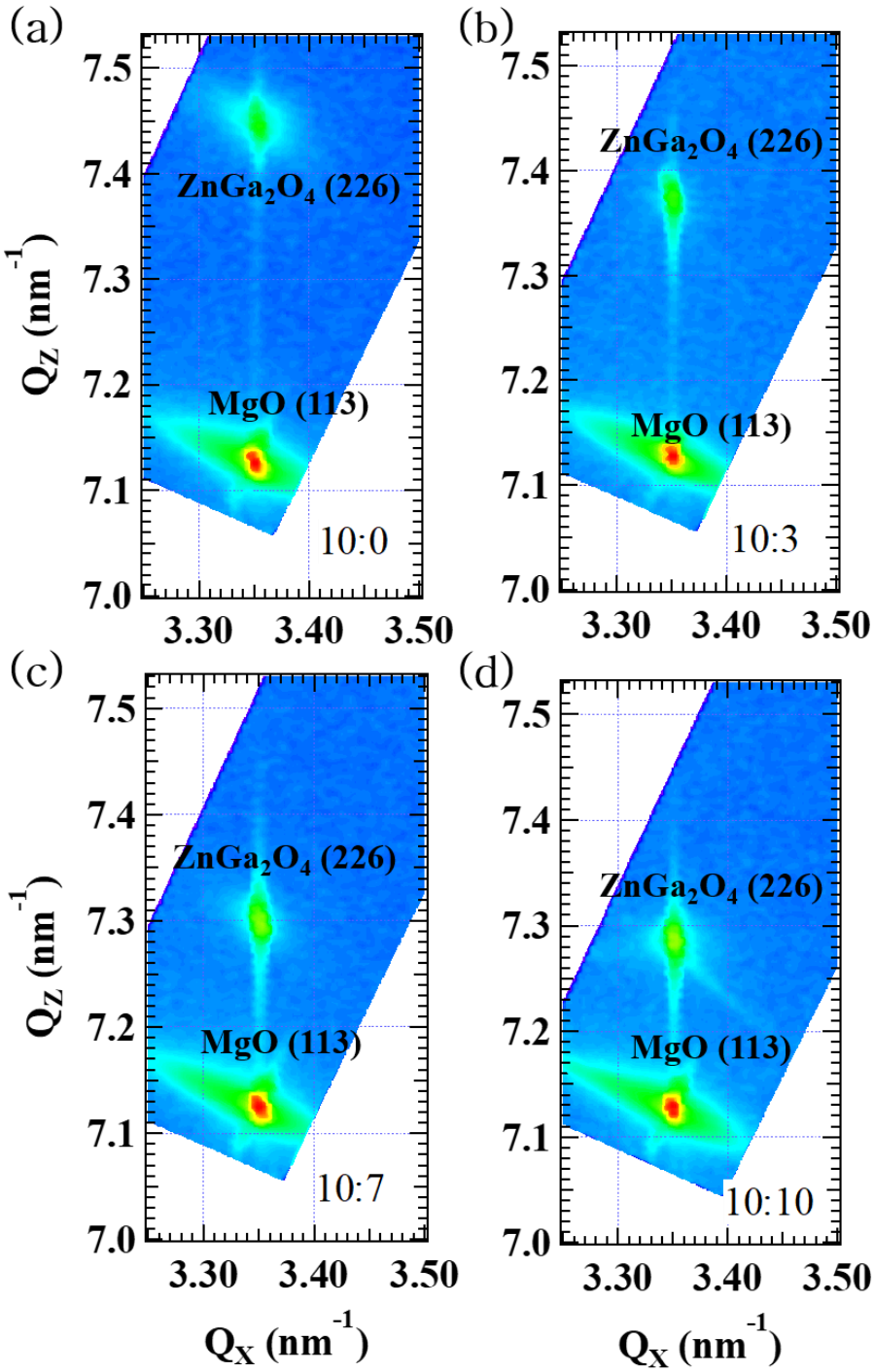

Figure 4.16. RSM of ZGO thin films on MgO (100). ZGO with (a) 10:0, (b) 10:3, (c) 10:7, and (d) 10:10

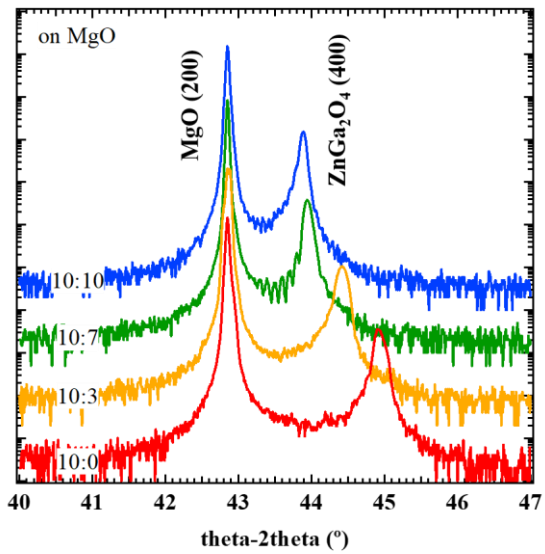

Figure 4.17. Theta-2theta scan of ZGO films on MgO substrates depending on the ZGO:ZnO shot ratio.

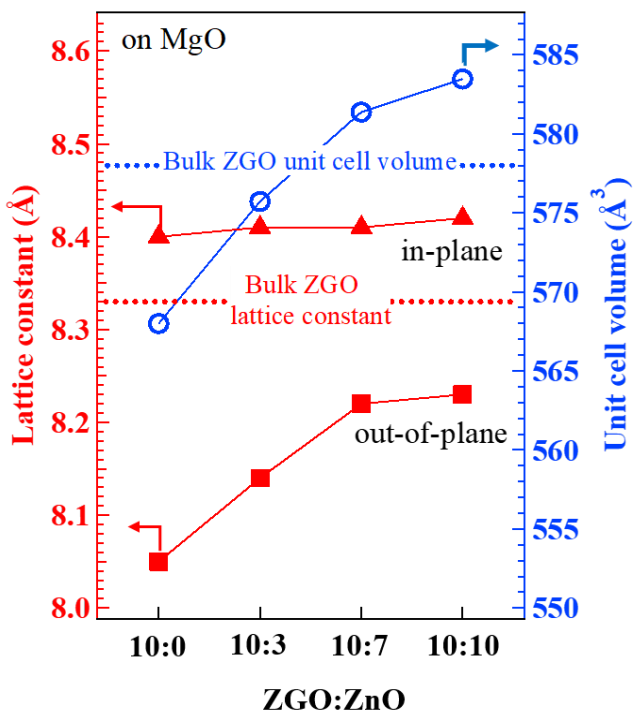

Figure 4.18. The lattice constants and unit cell volumes of ZGO on MgO (100) depending on ZGO:ZnO shot ratio.

than the bulk ZGO, while the unit cell volume at the 10:3 ratio is less than 1 % smaller than the bulk value. Starting from the 10:7 ratio, the ZGO thin films on MgO have larger unit cell volume than the bulk ZGO.

As the ZGO films on MAO, the interference fringes at both sides of ZGO peaks of RSM (Figure 4.16) and theta-2theta scan (Figure 4.17) were observed, implying the smooth surfaces of the ZGO films on MgO substrates. This was confirmed by using AFM. Figure 4.19 exhibits the smooth surfaces and RMS surface roughnesses of the ZGO films on MgO were under 290 pm.

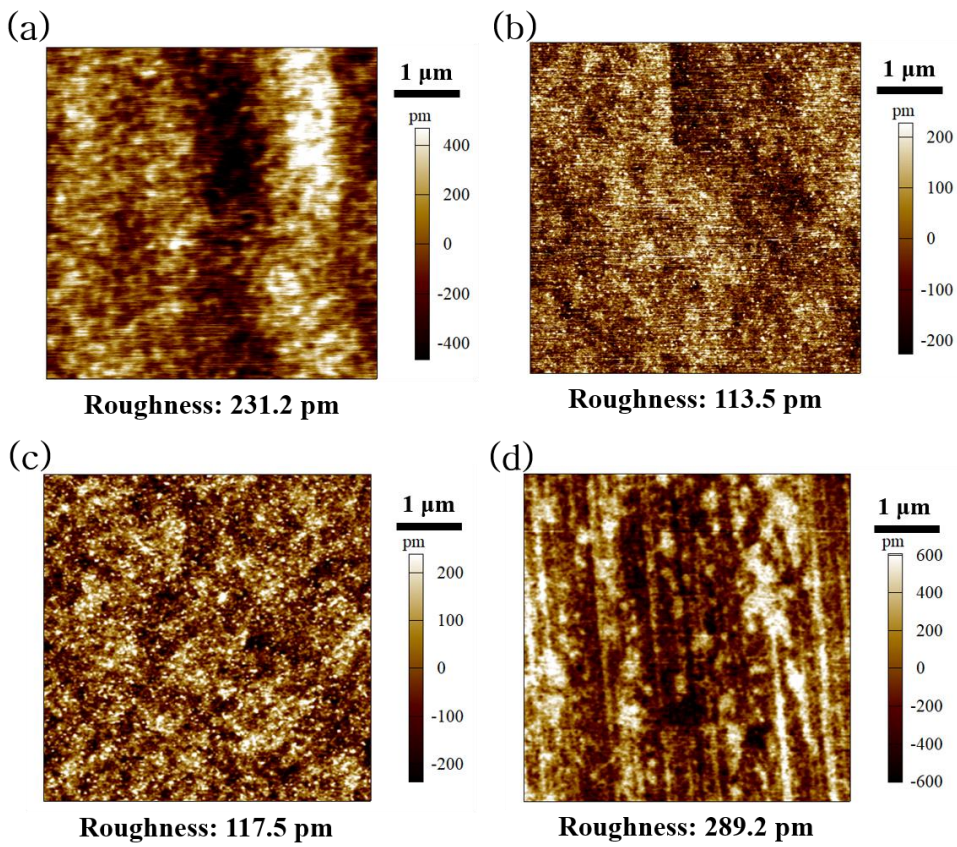

Figure 4.19. AFM images and surface roughness of ZGO thin films on MgO depending on ZGO:ZnO shot ratio of (a) 10:0, (b) 10:3, (c) 10:7, and (d) 10:10.

The Zn-Ga compositional ratios on MgO substrate depending on ZGO:ZnO shot ratio were also confirmed by EDS with SEM (Figure 4.20). The Zn/Ga ratio were 0.11 and 0.25 for ZGO:ZnO = 10:0 and 10:3, respectively. For 10:0 and 10:3 shot ratios, Zn was significantly deficient. At the 10:7 ratio, the substrate seems to make some difference; the Zn/Ga values in ZGO thin film are 0.45 on MgO and 0.41 on MAO substrates, respectively. The Zn/Ga value at 10:10 was 0.51 which is more Zn than the ideal value.

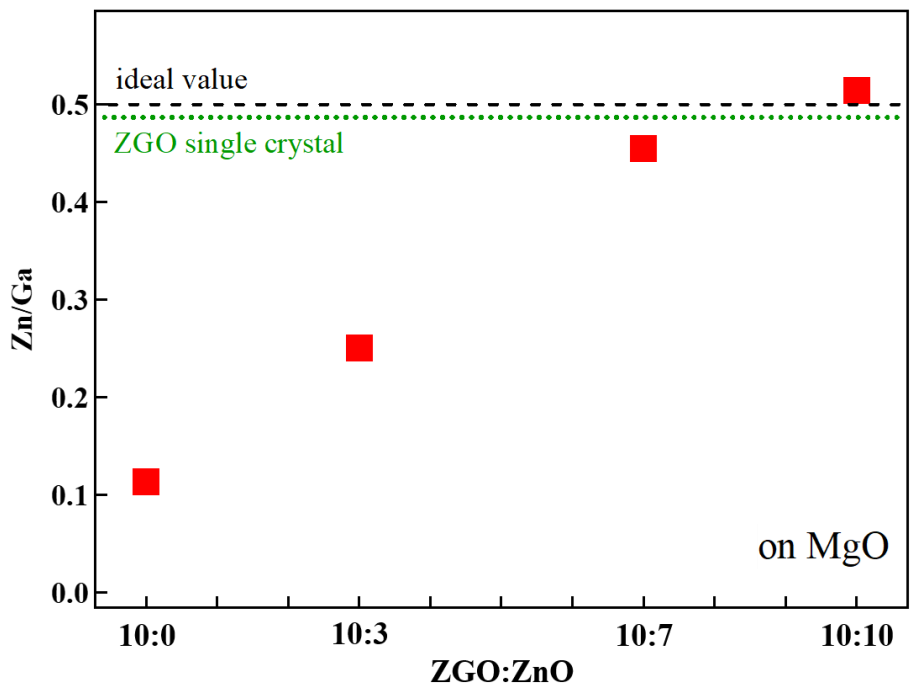

Figure 4.20. Zn-Ga compositional ratio on MgO substrate measurement by EDS with SEM.

Despite the severe deficiency of Zn in ZGO thin films on MAO and MgO substrates in 10:0 and 10:3 conditions, such ZGO thin films still show very good crystallinity without any sign of forming other phases, such as Ga_2O_3. The sustenance of ZGO single-crystal structure with a large deviation from the nominal cation compositional ratio is consistent with the previous ZGO single-crystal study [8]. The possible explanations could be provided by the antisite defect formation where the Zn site is occupied by Ga (Ga_{Zn}) and/or the Zn vacancies (V_{Zn}). It is also worth noting that despite almost the same Zn/Ga ratio on both substrates with each ZGO:ZnO ratio, there exists a large difference in the unit cell volumes on each substrate, suggesting that the strain state in thin films may have a large effect on the defect states.

The microstructure of the ZGO thin film on MgO was also checked by using TEM. Figure 4.21 exhibits the high-resolution TEM image of the cross-section of the 10:7 ZGO film on MgO substrate. The image of the interface between the ZGO film and the MgO substrate in Figure 4.21 (a) is showing coherent epitaxial growth without any dislocations. This is almost the same as the ZGO film on MAO substrates except for the blurred spots caused by the applied ion beam process and the difference in hardness between the ZGO thin film and the MgO substrate.

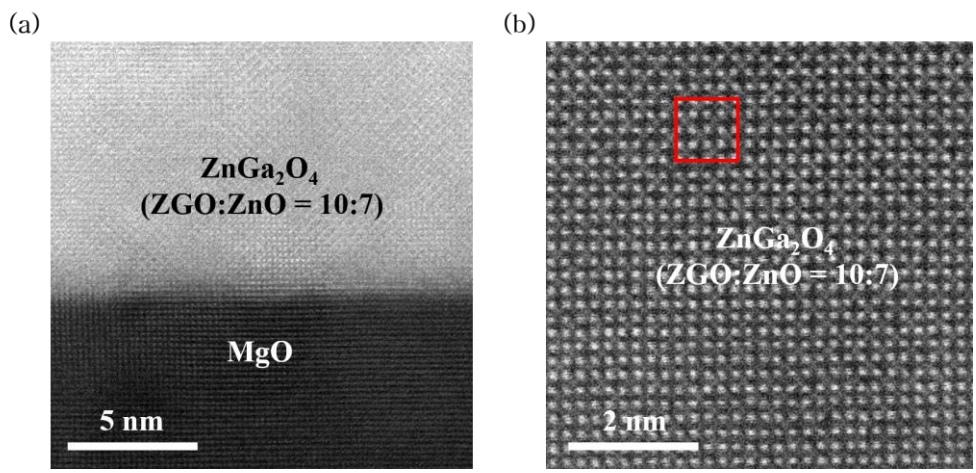

Figure 4.21. TEM images of ZGO on a MgO. (a) ZGO (ZGO:ZnO = 10:7) interface with MgO substrate. (b) ZGO (ZGO:ZnO = 10:7) away from the interface. Red rectangle in (b) represents a ZGO unit cell.

Unlike ferrite and chromite spinels on MgO substrates [72, 73, 92], the ZGO thin films are completely coherent on MgO substrates without any misfit dislocations. Although the misfit dislocations were not observed, there is a possibility of anti-phase boundaries in ZGO on MgO substrate like chromite spinels on MgO [92]. Since the unit cell of ZGO is twice as large as that of MgO, this could cause anti-phase boundaries by shifting a half unit cell in ZGO while maintaining coherent epitaxy without dislocations. This was not observed through the current TEM and RSM measurements. The higher-resolution TEM image (Figure 4.21 (b)) shows a ZGO unit cell which is representing a red rectangle in Figure 4.21 (b). Considering the brightest dots representing Ga and the light grey dots representing Zn, the edge-shared GaO_6 in ZGO appear to follow the edge-shared MgO_6 in the MgO substrate.

In addition to the absence of dislocations, the ZGO thin films on MgO exhibited the following low FWHM (full width at half maximum) values of rocking curves using XRD: 0.03 ~ 0.05 degree for 10:0 ~ 10:10 shot ratio films. These values are much lower than the previously reported ZGO thin films on MgO substrates [82, 94], exhibiting the improved crystallinity.

4.3 $ZnGa_2O_4$ thin film transistors: electrical transport properties

To evaluate the electrical transport properties of ZGO, the ZGO thin film transistors (TFTs) were fabricated depending on the ZGO:ZnO shot ratio on both MAO and MgO substrate type. For TFT fabrication, Al_2O_3 and ITO were used as gate oxide and source, drain, and gate electrodes, respectively. Before the ZGO TFT demonstration, Al_2O_3 dielectric properties were checked through Al_2O_3 capacitor with ITO electrodes. From the capacitance-frequency measurement (Figure 4.22. (a)), the calculated Al_2O_3 dielectric constant after post-ALD annealing process was 9 which is consistent with the previously reported values [31]. From the voltage-current measurement (Figure 4.22. (b)), it was checked that Al_2O_3 possesses over 4 MV/cm breakdown field.

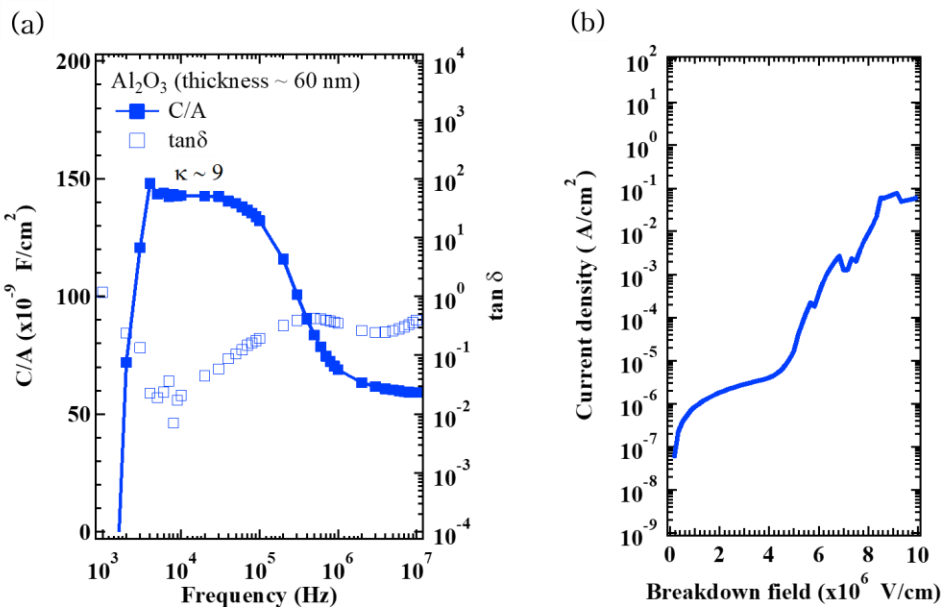

Figure 4.22. Al_2O_3 capacitor with ITO electrodes. (a) Capacitance-Frequency measurement. The calculated dielectric constant from capacitance per unit area was 9. (b) Breakdown field from a current-voltage measurement.

During the ALD deposition process for gate oxide, it was found that the originally insulating ZGO layer becomes slightly conducting. This seems due to the hydrogen doping [8, 24] of ZGO during the ALD process, probably coming from both TMA (trimethylaluminum, C_3H_9Al) and H_2O sources. This slight conduction change survived the following post-ALD annealing in oxygen. The conduction by this hydrogen doping is larger near the ZGO:ZnO = 10:7 condition. When the Zn/Ga ratio deviates too much from the 10:7 condition, it was found that the conduction of the channel after the Al_2O_3 gate oxide formation decreases.

Besides the Al_2O_3 dielectric properties, ITO optical property was examined through optical bandgap measurement. The ITO grown by PLD possesses a bandgap of 3.97 eV (Figure 4.23). Besides UV transparent ZGO (E_g: 4.6 ~ 5.2 eV) channel [8-10], Al_2O_3 (E_g: 8.8 eV) [31] gate oxide, and MAO (E_g > 7 eV) [95]/MgO (E_g ~ 7 eV) [92] substrates, it was possible to fabricate the near UV ~ UV transparent TFTs by using the ITO as electrodes.

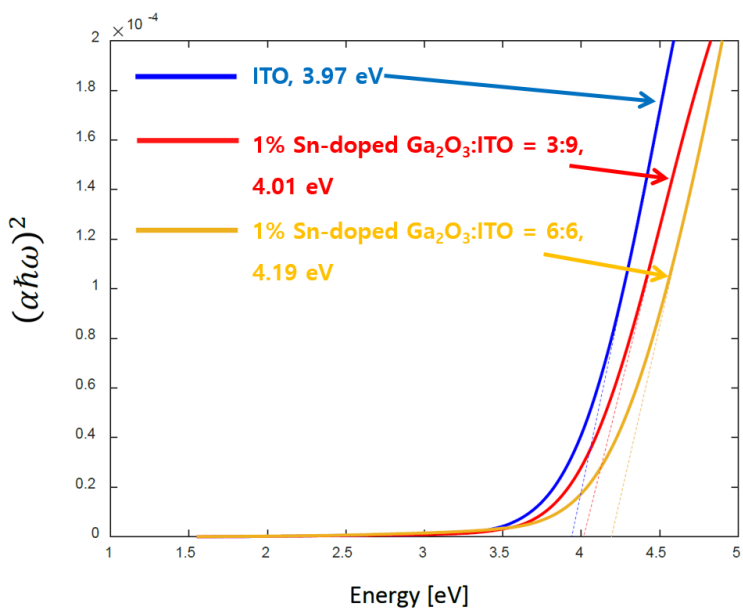

Figure 4.23. Optical bandgap measurement results of ITO deposited by using PLD.

Figure 4.24 displays the ZGO TFTs structures on MAO and MgO substrates. For each of the TFTs, I_{DS}-V_{DS} (output characteristics) and I_{DS}-V_{GS} (transfer characteristics) curves in the linear region (V_{DS} = 1 V) were measured.

ZGO TFT fabrications were tried with c-Al_2O_3 substrate. The ZGO TFTs on c-Al_2O_3 exhibited the very low field effect mobility less than 0.05 cm^2/Vs with a large hysteresis curve. Considering the ZGO thin film structural properties on c-Al_2O_3, these poor electric properties seem to originate from the grain boundaries of ZGO. From the results, the ZGO TFT investigation was only focused on using MAO and MgO substrates.

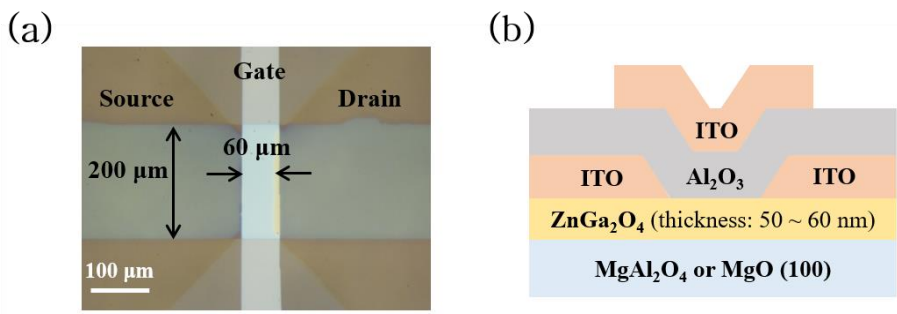

Figure 4.24. ZGO TFT structure on MAO and MgO substrates. (a) Top view optical microscope image. (b) Illustration of cross-section schematic.

4.3.1 Thin film transistors on $MgAl_2O_4$

Figure 4.25 shows the electrical characteristics of TFTs on MAO with 10:0 and 10:7 conditions. The output curves in Figure 4.25 (a) and (c) affirm the n-type TFTs on MAO substrates. The transfer characteristics were measured in the linear region (V_{DS} = 1 V), as shown in Figure 4.25 (b) and (d). From the measurements, the field effect mobility (μ_{FE}), I_{ON}/I_{OFF} ratio, and subtrhreshold swing (S) were obtained. As increase ZGO:ZnO shot ratio from 10:0 to 10:7, the ZGO TFTs exhibited better TFT characteristics of higher mobility of 0.1 cm^2/Vs and larger I_{ON}/I_{OFF} ratio of 1.2×10^7. S-value was 1.48 V/dec for 10:7 TFT.

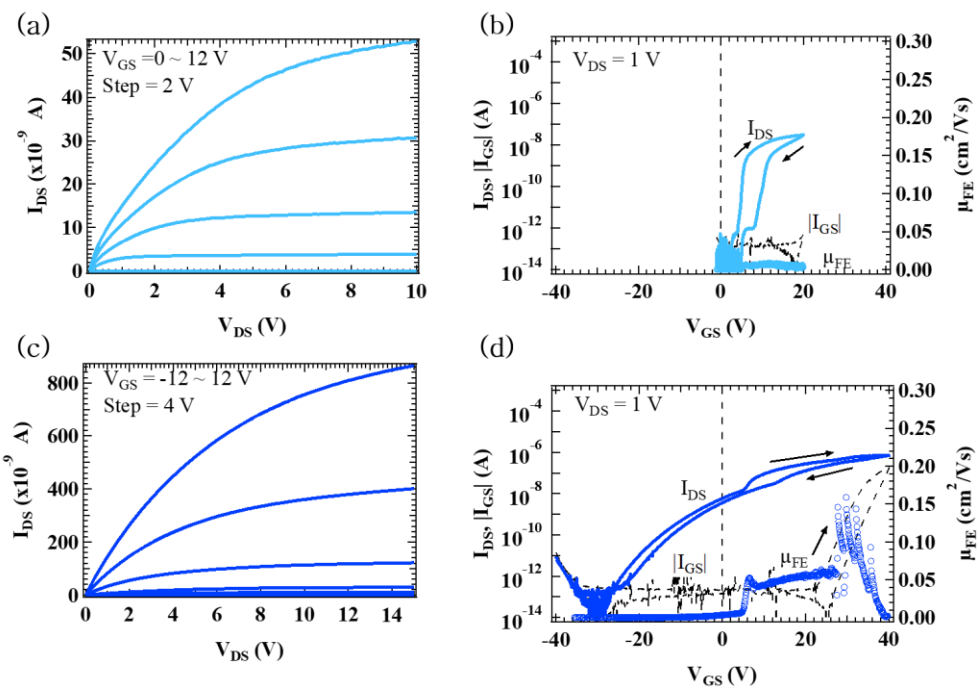

Figure 4.25. ZGO TFT performances depending on the ZGO:ZnO shot ratio on MAO substrates. (a) Output characteristics based on ZGO:ZnO = 10:0. (b) Transfer characteristics based on ZGO:ZnO = 10:0. (c) Output characteristics based on ZGO:ZnO = 10:7. (b) Transfer characteristics based on ZGO:ZnO = 10:7.

4.3.2 Thin film transistors on MgO

Figure 4.26 shows the output characteristics and transfer characteristics of the ZGO TFTs on MgO substrates depending on the channel condition. Regardless of the channel conditions of ZGO:ZnO shot ratio, the output characteristics (Figure 4.26 (a), (c), (e), (g), (i), (k) and (m)) verify the n-type TFTs on MgO substrates. From transfer characteristics (Figure 4.26 (b), (d), (f), (h), (j), (l) and (n)) measured in the linear region (V_{DS} = 1 V), μ_{FE}, I_{ON}/I_{OFF} ratio, and S-values were obtained for each ZGO channel condition. Including the ZGO TFTs on MAO substrates, all TFTs show a clockwise hysteresis curve that usually arises from the electron trap states at the channel-gate insulator interface for n-type TFTs [58]. As comparing with 10:7 TFT on MAO substrate, 10:7 channel TFT on MgO showed the better properties of μ_{FE}= 3.9 cm^2/Vs, I_{ON}/I_{OFF} ratio = 3.3×10^8, and S-value = 0.11 V/dec. In all aspects, the TFTs exhibit the improved performances on the MgO substrates, suggesting that the tensile strain in the ZGO films affects the electrical properties to a lesser extent than the compressive strain does. It is also clear that the cation compositional ratio has a significant impact on electrical transport properties. The mobility increases with the Zn/Ga ratio and it reaches its maximum value near the ZGO:ZnO = 10:7 shot ratio. With a 10:6 shot ratio on a MgO substrate, the TFT (Figure 4.26 (g) and (h)) exhibited the highest mobility of 5.4 cm^2/Vs and the highest I_{ON}/I_{OFF} ratio of 4.5×10^8. The S-value was 0.19 V/dec. In the case of the 10:8 ratio as Zn/Ga ratio was further increased, the mobility started to remarkably decrease. When the ZGO has a slightly smaller Zn/Ga ratio than the theoretically stoichiometric value, in the ZGO:ZnO shot range between 10:5 and 10:7, ZGO TFTs seem to show the best electrical properties.

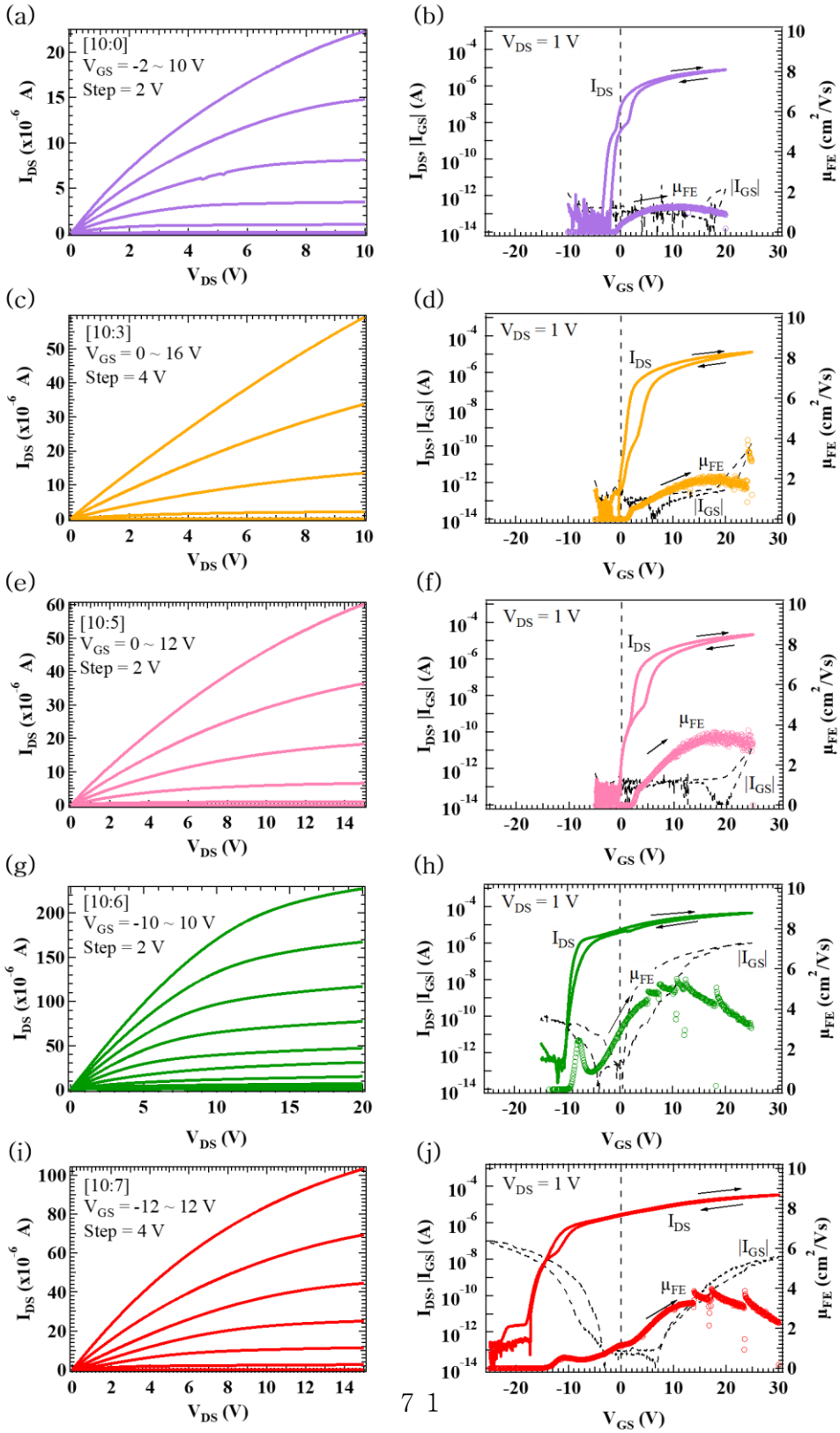
(a)
[10:0]
V_{GS} = -2 ~ 10 V
Step = 2 V
I_{DS} (x10^{-6} A)
V_{DS} (V)
(b)
V_{DS} = 1 V
I_{DS}
μ_{FE}
$|I_{GS}|$
I_{DS}, $|I_{GS}|$ (A)
μ_{FE} (cm^2/Vs)
V_{GS} (V)
(c)
[10:3]
V_{GS} = 0 ~ 16 V
Step = 4 V
I_{DS} (x10^{-6} A)
V_{DS} (V)
(d)
V_{DS} = 1 V
I_{DS}
μ_{FE}
$|I_{GS}|$
I_{DS}, $|I_{GS}|$ (A)
μ_{FE} (cm^2/Vs)
V_{GS} (V)
(e)
[10:5]
V_{GS} = 0 ~ 12 V
Step = 2 V
I_{DS} (x10^{-6} A)
V_{DS} (V)
(f)
V_{DS} = 1 V
I_{DS}
μ_{FE}
$|I_{GS}|$
I_{DS}, $|I_{GS}|$ (A)
μ_{FE} (cm^2/Vs)
V_{GS} (V)
(g)
[10:6]
V_{GS} = -10 ~ 10 V
Step = 2 V
I_{DS} (x10^{-6} A)
V_{DS} (V)
(h)
V_{DS} = 1 V
I_{DS}
$|I_{GS}|$
μ_{FE}
I_{DS}, $|I_{GS}|$ (A)
μ_{FE} (cm^2/Vs)
V_{GS} (V)
(i)
[10:7]
V_{GS} = -12 ~ 12 V
Step = 4 V
I_{DS} (x10^{-6} A)
V_{DS} (V)
(j)
V_{DS} = 1 V
I_{DS}
$|I_{GS}|$
μ_{FE}
I_{DS}, $|I_{GS}|$ (A)
μ_{FE} (cm^2/Vs)
V_{GS} (V)

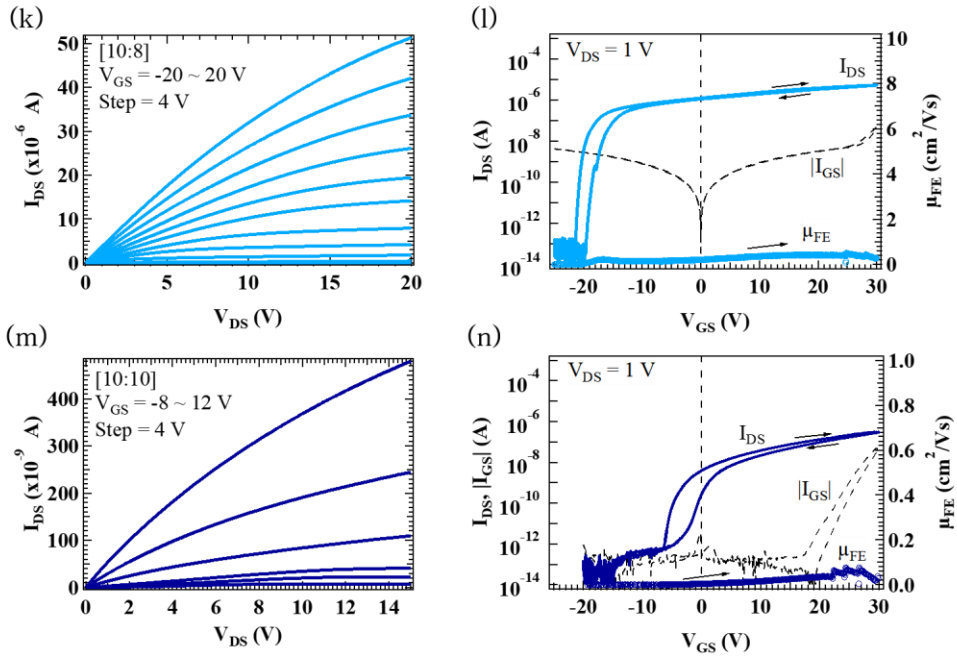

Figure 4.26. ZGO TFT on MgO substrates performances depending on the ZGO:ZnO shot ratio. Output characteristics of (a) 10:0, (c) 10:3, (e) 10:5, (g) 10:6, (i) 10:7, (k) 10:8, and (m) 10:10. Transfer characteristics of (b) 10:0, (d) 10:3, (f) 10:5, (h) 10:6, (j) 10:7, (l) 10:8, and (n) 10:10.

4.3.3 Electrical properties: antisite defects and vacancies

Such results of showing the best electrical transport properties range of 10:5 ~ 10:7 are consistent with the previous report on the ZGO single crystals [8]. In spinel oxide materials (AB_2O_4), the prevalent defects are antisite defects (B_A and A_B). Despite the low degree of inverse spinel formation in ZGO [79], there is a possibility to form antisite defects. For stoichiometric $ZnGa_2O_4$, the possible defects occur in the order of antisite defects (Ga_{Zn} and Zn_{Ga}), oxygen vacancies (V_O), Zn vacancies(V_{Zn}), and Ga vacancies (V_{Ga}). Among the defects, the most prominent antisite defects of Ga_{Zn} acting for donor and Zn_{Ga} acting for acceptor compensate each other [96, 97]. Therefore, the self-doping effect or electrical properties change could be not observed for stoichiometric $ZnGa_2O_4$.

However, for the low temperature (450 ℃) deposited ZGO with the slight Zn deficiency, Ga_{Zn} and V_{Zn} seem to be dominant defects and result in the showing the highest mobility at Zn deficient ZGO condition (ZGO:ZnO = 10:5 ~ 10:7). In ZGO where the Ga ions are known to form GaO_4 tetrahedra (for example, in β-Ga_2O_3) with little possibility of ZnO_6 octahedra, the Ga_{Zn} antisite defect is likely to form, especially during the low temperature thin film growth. However, with a high Ga_{Zn} defect density, which should act as donors, any doping effect in ZGO films was not observed, suggesting that V_{Zn} defects, which act as compensating acceptors, may accompany the Ga_{Zn} antisite defects. Furthermore, as adding more Zn beyond the 10:7 ratio, the additional Zn may create Zn_{Ga} defects instead of reducing the Ga_{Zn} and V_{Zn} defects density, which can explain the observed decrease of the mobility. [96, 97]

Based on TFT results, the electrical conductivities depending on ZGO:ZnO shot ratio and substrate were marked in Figure 4.27. Red squares filled with + mark represent the ZGO TFTs on MAO substrates and red squares filled with × mark represent the ZGO TFTs on MgO substrates. The electric properties of ZGO on each substrates

represent the 3 dimensional carrier densities at the highest mobility which is varying by applying an electric field. When the ZGO TFT showed the highest mobility (10:6 channel on a MgO substrate), the electrical conductivity is obtained the highest value of 0.1 $\Omega^{-1}\cdot cm^{-1}$. As shown in Figure 4.27, the ZGO thin film on the MgO substrate exhibits higher electric properties than the ZGO thin film on c-Al_2O_3 [10].

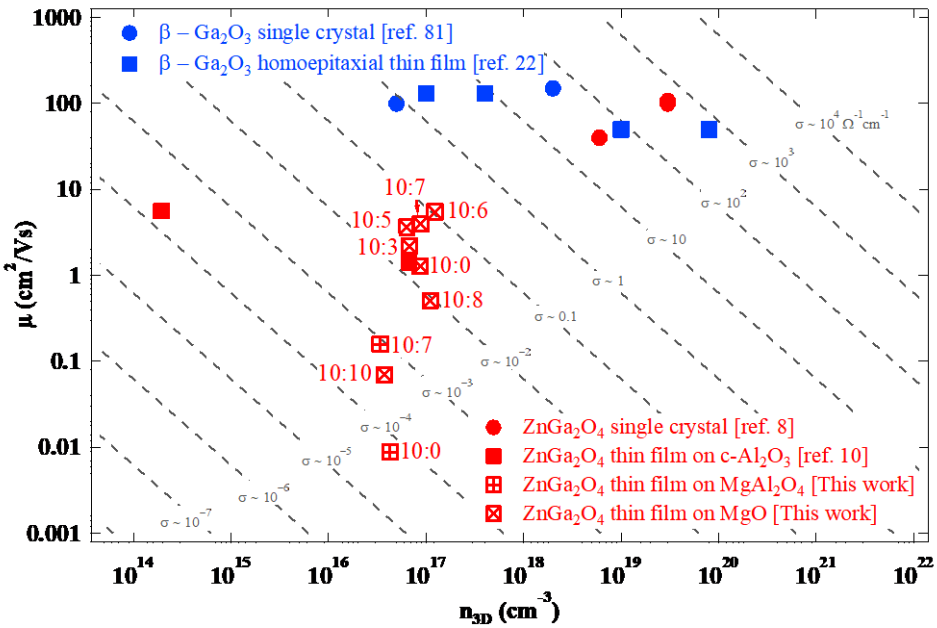

Figure 4.27. Mobility against carrier density of $ZnGa_2O_4$ (single crystal, thin film on c-Al_2O_3, thin film on MAO, and thin film on MgO) and β-Ga_2O_3 [8, 10, 22, 81].

In summary, using the coherently epitaxial spinel $ZnGa_2O_4$ films on $MgAl_2O_4$ and MgO substrates, the structural and compositional effect of the ZGO:ZnO shot ratio in the PLD process were studied by examining thin films. Based on film studies, UV transparent ZGO thin film transistors were fabricated and measured. From the TFTs properties, the TFTs made with slightly less than Zn/Ga =0.5 on the MgO substrates (tensile strain) showed the best electrical properties.

There is a possibility of anti-phase boundaries in ZGO on the MgO substrate since the unit cell of ZGO is twice as large as that of MgO, which can cause boundaries by shifting a half unit cell in ZGO whiled maintaining coherent epitaxy without dislocations.[73, 93] More understanding of such defects, as well as the hydrogen dopant, will be helpful in further enhancing the mobility to a value closer to that observed in bulk ZGO single crystals [8]. Along with the defects and doping understanding, if it is possible to demonstrate ZGO homoepitaxial thin film, it is expected that verifying high ZGO electrical conductivity over β-Ga_2O_3 homoepitaxial thin film.

Bibliography

[1] T. Fung, C. Chuang, K. Nomura, H. D. Shieh, H. Hosono, and J. Kanicki, J. Inf. Disp. **9**, 21 (2008).

[2] H. Kim, U. Kim, T. H. Kim, J. Kim, H. M. Kim, B. Jeon, W. Lee, H. S. Mun, K. T. Hong, J. Yu, K. Char, and K. H. Kim, Phys. Rev. B **86**, 165205 (2012).

[3] V. Srikant and D. R. Clarke, J. Appl. Phys. **83**, 5447 (1998).

[4] J. Y. Tsao, S. Chowdhury, M. A. Hollis, D. Jena, N. M. Johnson, K. A. Jones, R. J. Kaplar, S. Rajan, C. G. Van de Walle, E. Bellotti, C. L, Chua, R. Collazo, M. E. Coltrin, J. A. Cooper, K. R. Evans, S. Graham, T. A. Grotjohn, E. R. Heller, M. Higashiwaki, M. S. Islam, P. W. Juodawlkis, M. A. Khan, A. D. Koehler, J. H. Leach, U. K. Mishra, R. J. Nemanich, R. C. N. Pilawa-Podgurski, J. B. Shealy, Z. Sitar, M. J. Tadjer, A. F. Witulski, M. Wraback, and J. A. Simmons, Adv. Electron. Mater. **4**, 1600501 (2018).

[5] T. Tharsika, A. S. M. A. Haseeb, S. A. Akbar, M. F. M. Sabri, and W. Y. Hoong, Sensors **14**, 14586 (2014).

[6] M. Wei, A. V. Sanchela, B. Feng, Y. Ikuhara, H. J. Cho, and H. Ohta, Appl. Phys. Lett. **116**, 022103 (2020).

[7] C. Janowitz, V. Scherer, M. Mohamed, A. Krapf, H. Dwelk, R. Manzke, Z. Galazka, R. Uecker, K. Irmscher, R. Fornari, M. Michling, D. Schmeiber, J. R. Weber, J. B. Varley, and C. G. Van de Walle, New J. Phys. **13**, 085014 (2011).

[8] Z. Galazka, S. Ganschow, R. Schewski, K. Irmscher, D. Klimm, A. Kwasniewski, M. Pietsch, A. Fiedler, I. Schulze-Jonack, M. Albrecht, T. Schroder, and M. Bickermann, APL Mater. **7**, 022512 (2019).

[9] T. Oshima, M. Niwa, A. Mukai, T. Nagami, T. Suyama, and A. Ohtomo, J. Cryst. Growth **386**, 190 (2014).

[10] R. Horng, C. Huang, S. Ou, T. Juang, and P. Liu, Cryst. Growth Des. **17**, 6071 (2017).

[11] H. Hosono, Thin Solid Films **515**, 6000 (2007).

[12] L. Xiang, J. L. Palma, Y. Li, V. Mujica, M. A. Ratner, and N. Tao, Nat. Commun. **8**, 14471 (2017).

[13] M. Higashiwaki, K. Sasaki, A. Kuramata, T. Masui, And S. Yamakoshi, Appl.

Phys. Lett. **100**, 013504 (2012).
[14] B. J. Baliga, IEEE Electron Device Lett. **10**, 455 (1989).
[15] U. K. Mishra, P. Parikh, and Y. Wu, P. IEEE **90**, 1022 (2002).
[16] H. Amano, A. Miyazaki, K. Iida, T. Kawashima, M. Iwaya, S. Kamiyama, I. Akasaki, R. Liu, A. Bell, and F. Ponce, Phys. Status Solidi A **201**, 2679 (2004).
[17] K. Ban, J. Yamamoto, K. Takeda, K. Ide, M. Iwaya, T. Takeuchi, S. Kamiyama, I. Akasaki, and H. Amano, Appl. Phys. Express **4**, 052101 (2011).
[18] Z. Bryan, I. Bryan, J. Xie, S. Mita, Z. Sitar, and R. Collazo, Appl. Phys. Lett. **106**, 142107 (2015).
[19] M. Iwaya, S. Terao, T. Sano, S. Takanami, T. Ukai, R. Nakamura, S. Kamiyama, H. Amano, and I. Akasaki, Phys. Status Solidi A **188**, 117 (2001).
[20] J. Isberg, J. Hammersberg, E. Johansson, T. Wikstrom, D. J. Twitchen, A. J. Whitehead, S. E. Coe, and G. A. Scarsbrook, Science **297**, 1670 (2002).
[21] C. J. H. Wort and R. S. Balmer, Mater. Today **11**, 22 (2008).
[22] M. Baldini, M. Albrecht, A. Fiedler, K. Irmscher, R. Schewski, and G. Wagner, ECS J. Solid State Sci. Technol. **6**, Q3040 (2016).
[23] S. J. Pearton, J. Yang, P. H. Cary, F. Ren, J. Kim, M. J. Tadjer, and M. A. Mastro, Appl. Phys. Rev. **5**, 011301 (2018).
[24] T. Omata, N. Ueda, and K. Ueda, Appl. Phys. Lett. **64**, 1077 (1994).
[25] R. F. Pierret, Semiconductor Device Fundamentals, Addison Wesley (1996).
[26] J. F. Wagger, D. A. Keszler, R. E. Presley, Transparent Electronics, Springer (2008).
[27] C. Ju, C. Park, H. Yang, U. Kim, Y. M. Kim, and K. Char, Curr. Appl. Phys. **16**, 300 (2016).
[28] H. Mun, H. Yang, J. Park, C. Ju, and K. Char, APL Mater. **3**, 076107 (2015).
[29] R. W. Johnson, A. Hultqvist, S. F. Bent, Mater. Today **17**, 236 (2014).
[30] Y. Shen, C. Tung, C. Huang, Y. Lin, Y. Lin, and R. Horng, ACS Appl. Electron. Mater. **1**, 783 (2019).
[31] J. Robertson, Eur. Phys. J. Appl. Phys. **28**, 265 (2004).
[32] K. Nomura, H. Ohta, K. Ueda, T. Kamiya, M. Hirano, and H. Hosono, Science **300**, 1269 (2003).

[33] K. Nomura, H. Ohta, A. Takagi, T. Kamiya, M. Hirano, and H. Hosono, Nature **432**, 488 (2004).

[34] P. Chen and H. Jeng, Sci. Rep. **5**, 16539 (2015).

[35] Y. Ogo, H. Hiramatsu, K. Nomura, H. Yanagi, T. Kamiya, M. Hirano, and H. Hosono, Appl. Phys. Lett. **93**, 032113 (2008).

[36] R. Martins, A. Nathan, R. Barros, L, Pereira, P. Barquinha, N. Correia, R. Costa, A. Ahnood, I. Ferreira, and E. Fortunato, Adv. Mater. **23**, 4491 (2011).

[37] J. Gong, X. Wang, X. Fan, R. Dai, Z. Wang, Z. Zhang, and Z. Ding, Opt. Mater. Express **9**, 3691 (2019).

[38] X. Feng, J. Ma, F. Yang, F. Ji, F. Zong, C. Luan, and H. Ma, Appl. Surf. Sci. **254**, 6601 (2008).

[39] E. Cetinorgu and S. Goldsmith, J. Phys. D: Appl. Phys. **40**, 5220 (2007).

[40] A. Tricoli, M. Graf, and S. E. Pratsinis, Adv. Funct. Mater. **18**, 1969 (2008).

[41] C. Kilic and A. Zunger, Phys. Rev. Lett. **88**, 095501 (2002).

[42] H. Kim and A. Pique, Appl. Phys. Lett. **84**, 218 (2004).

[43] H. Kim, R. C. Y. Auyeung, and A. Pique, Thin Solid Films **516**, 5052 (2008).

[44] H. Toyosaki, M. Kawasaki, and Y. Tokura, Appl. Phys. Lett. **93**, 132109 (2008).

[45] S. Das and V. Jayaraman, Prog. Mater. Sci. **66**, 112 (2014).

[46] M. Nagasawa, S. Shionoya, and S. Makishima, Jap. J. Appl. Phys. **4**, 195 (1965).

[47] J. Sun, A. Lu, L. Wang, Y. Hu, and Q. Wan, Nanotechnology **20**, 335204 (2009).

[48] G. Huang, L. Duan, G. Dong, D. Zhang, and Y. Qiu, ACS Appl. Mater. Interfaces **6**, 20786 (2014).

[49] J. Jang, R. Kitsomboonloha, S. L. Swisher, E. S. Park, H. Kang, and V. Subramanian, Adv. Mater. **25**, 1042 (2013).

[50] C. W. Shih, A. Chin. C. F. Lu, and W. F. Su, Sci. Rep. **6**, 19023 (2016).

[51] C. W. Shih and A. Chin, ACS Appl. Mater. Interfaces **8**, 19187 (2016).

[52] Y. M. Kim, C. Park, U. Kim, C. Ju, and K. Char, Appl. Phys. Express **9**, 011201 (2016).

[53] D. Kang, H. Lim, C. Kim, I. Song, J. Park, and Y. Park, Appl. Phys. Lett. **90**, 192101 (2007).

[54] C. Bae, D. Kim, S. Moon, T. Choi, Y. Kim. B. S. Kim, J. Lee, H. Shin, and J.

Moon, ACS Appl. Mater. Interfaces **2**, 626 (2010).
[55] J. Gope, Vandana, N. Batra, J. Panigrahi, R. Singh, K. K. Maurya, R. Srivastava and P. K. Singh, Appl. Surf. Sci. **357**, 635 (2015).

[56] X. Wang, W. Hu, X. Chen, and W. Lu, IEEE Trans. Electron Devices **59**, 1393 (2012).

[57] V. O. Turing and A. A. Balandin, J. Appl. Phys. **100**, 054501 (2006).
[58] M. Egginger, S. Bauer, R. Schwodiauer, H. Neugebauer, and N. S. Sariciftci, Monatsh. Chem. **140**, 735 (2009).
[59] W. Xu, M. Dai, L. Liang, Z. Liu, X. Sun, Q. Wan, and H. Cao, J. Phys. D: Appl. Phys. **45**, 205103 (2012).
[60] S. Kolliopoulou, P. Dimitrakis, P. Normand, H. Zhang, N. Cant, S. D. Evans, S. Paul, C. Pearson, A. Molloy, M. C. Pettyto, and D. Tsoukalas, J. Appl. Phys. **94**, 5234 (2003).
[61] J. Muller, P. Polakowski, S. Mueller, and T. Mikolajick, ECS J. Solid State Sci. Technol. **4**, N30 (2015).
[62] C. Lee, E. Cho, H. Lee, C. S. Hwang, and S. Han, Phys. Rev. B **78**, 012102 (2008).
[63] J. Muller, T. S. Boscke, U. Schroder, S. Mueller, D. Brauhaus, U. Bottger, L. Frey, and T. Mikolajick, Nano Lett. **12**, 4318 (2012).
[64] P. Polakowski and J. Muller, Appl. Phys. Lett. **106**, 232905 (2015).
[65] K. D. Kim, M. H. Park, H. J. Kim, Y. J. Kim, T. Moon, Y. H. Lee, S. D. Hyun, T. Gwon, and C. S. Hwang, J. Mater. Chem. C **4**, 6864 (2016).
[66] P. R. Bueno, J. A. Varela, and E. Longo, J. Eur. Ceram. Soc. **28**, 505 (2008).
[67] M. Batzill and U. Diebold, Prog. Surf. Sci. **79**, 47 (2005).
[68] E. R. Leite, A. M. Nascimento, P.R. Bueno, E. Longo, and J. A. Varela, J. Mater. Sci: Mater. Electron. **10**, 321 (1999).
[69] F. M. Hossain, J. Nishii, S. Takagi, A. Ohtomo, T. Fukumura, H. Fujioka, H. Ohno, H. Koinuma, and M. Kawasaki, J. Appl. Phys. **94**, 7768 (2003).
[70] J. E. Dominguez, L. Fu, and X. Q. Pan, Appl. Phys. Lett. **81**, 5168 (2002).
[71] D. C. Johnson, J. Low Temp. Phys. **25**, 145 (1976).

[72] H. Wu, O. Mauit, C. O. Coileain, A. Syrlybekov, A. Khalid, A. Mouti, M. Abid, H. Zhang, M. Abid, And I. V. Shvets, Sci. Rep. **4**, 7012 (2014).

[73] J. A. Heuver, A. Scaramucci, Y. Blickenstorfer, S. Matzen, N. A. Spaldin, C. Ederer, and B. Noheda, Phys. Rev. B **92**, 214429 (2015).

[74] C. Gatel, B. Warot-Fonrose, S. Matzen, and J. B. Moussy, Appl. Phys. Lett. **103**, 092405 (2013).

[75] Y. Yamasaki, S. Miyasaka, Y. Kaneko, J. P. He, T. Arima, and Y. Tokura, Phys. Rev. Lett. **96**, 207204 (2006).

[76] T. J. Coutts, X. Wu, W. P. Mulligan, and J. M. Webb, J. Electron. Mater. **25**, 935 (1996).

[77] Y. Wang, H. Zhang, L. Lin, S. Zhou, Y. Yao, X. Yang, and Y. Zhao, J. Appl. Phys. **125**, 095701 (2019).

[78] Y. Yang, J. Zhang, S. Hu, Yabei Wu, J. Zhang, W. Ren, and S. Cao, Phys. Chem. Chem. Phys. **19**, 28928 (2017).

[79] A. Seko, K. Yuge, F. Oba, A. Kuwabara, and I. Tanaka, Phys. Rev. B **73**, 184117 (2006).

[80] U. Kim, C. Park, T. Ha, R. Kim, H. S. Mun, H. M. Kim, H. J. Kim, T. H. Kim, N. Kim, J. Yu, K. H. Kim, J. H. Kim, and K. Char, APL Mater. **2**, 056107 (2014).

[81] S. J. Pearton, J. Yang, P. H. Cary, F. Ren, J. Kim, M. J. Tadjer, and M. A. Mastro, Appl. Phys. Rev. **5**, 011301 (2018).

[82] Y. E. Lee, D. P. Norton, and J. D. Budai, Appl. Phys. Lett. **74**, 3155 (1999).

[83] P. D. Rack, J. J. Peterson, M. D. Potter, and W. Park, J. Mater. Res. **16**, 1429 (2001).

[84] Z. Gu, F. Liu, X. Li, J. Howe, J. Xu, Y. Zhao, and Z. Pan, J. Phys. Chem. Lett. **1**, 354 (2010).

[85] Y. Shen, W. Wang, and R. Horng, IEEE J. Electron Devices Soc. **5**, 112 (2017).

[86] L. Cheng, C. Huang, and R. Horng, IEEE J. Electron Devices Soc. 6, 432 (2018).

[87] X. Liu, S. Middey, Y. Cao, M. Kareev, and J. Chakhalian, MRS Commun. **6**, 133 (2016).

[88] J. X. Ma, D. Mazumdar, G. Kim, H. Sato, N. Z. Bao, and A. Gupta, J. Appl. Phys. **108**, 063917 (2010).

[89] Y. Ma and X. Liu, Molecules **24**, 1704 (2019).
[90] V. Kapaklis, P. Poulopoulos, V. Karoutsos, Th. Manouras, and C. Politis, Thin Solid Films **510**, 138 (2006).
[91] J. G. Smith, J. Naruse, H. Hiramatsu, and D. J. Siegel, Chem. Mater. **29**, 3152 (2017).
[92] O. E. Tauria, M. Springbor, and N. E. Christensen, Solid State Commun. **55**, 351 (1985).
[93] R. Guzman, J. Heuver, S. Matzen, C. Magen, and B. Noheda, Phys. Rev. B **96**, 104105 (2017).
[94] Z. Yan, M. Koike, and H. Takei, J. Cryst. Growth **165**, 183 (1996).
[95] I. Ganesh, Int. Mater. Rev. **58**, 63 (2013).
[96] T. R. Paudel, A. Zakutayev, S. Lany, M. d'Avezac, and A. Zunger, Adv. Funct. Mater. **21**, 4493 (2011).
[97] Y. Shi, P. F. Ndione, L. Y. Lim, D. Sokaras, T.-C. Weng, A. R. Nagaraja, A. G. Karydas, J. D. Perkins, T. O. Mason, D. S. Ginley, A. Zunger, and M. F. Toney, Chem. Mater. **26**, 1867 (2014).

국문초록

이 논문은 박막트랜지스터를 이용하여 넓은 밴드갭 반도체인 주석산화물 (SnO_2) 과 아연갈륨산화물 ($ZnGa_2O_4$)을 연구하는데 초점을 두고 있다. 물질의 특성과, 투명 디스플레이 분야와 하이파워 디바이스 분야로의 응용 가능성을 확인하기 위해 각 물질의 박막과 박막 트랜지스터를 연구하였다. 특히 박막 트랜지스터를 이용할 경우 소자의 특성을 확인 할 수 있을 뿐만 아니라, 전기장을 통한 캐리어 변조가 가능하여 물질의 전기적 특성을 확인 할 수 있는 장점이 있다.

기존 반도체 물질인 Si, GaAS (밴드갭: 1 ~ 1.5 eV) 보다 큰 밴드갭을 갖는 반도체 물질들을 넓은 밴드갭 반도체라고 하며, 투명성과 높은 항복 전압을 갖는다. 가시광선 영역에 해당하는 3.1 eV 보다 큰 밴드갭을 갖는 물질의 경우 가시광선 영역에서 투명하다. 3.94 eV, 4.43 eV 보다 큰 밴드갭을 갖는 경우 물질들은 각각 자외선 A, 자외선 B 영역까지 투명한 특성을 보인다. 더불어, 밴드갭이 큰 물질일수록 충돌을 일으키는 캐리어 발생에 큰 전기장을 필요로 하기 때문에 큰 항복 전압을 갖는다. 이로부터 넓은 밴드갭 반도체는 디스플레이/광전자공학 분야 및 하이파워소자 분야에서 중요하게 다뤄지고 있다. 잘 알려진 넓은 밴드갭 반도체 물질로는 이 논문에서 연구된 주석산화물 (밴드갭 3.6 eV), 아연갈륨산화물 (밴드갭 4.6 ~ 5.2 eV) 외에 IGZO (밴드갭 3.0 eV), $BaSnO_3$ (밴드갭 3.1 eV), ZnO (밴드갭 3.3 eV), SiC (밴드갭 3.3 eV), $SrSnO_3$ (밴드갭 4.6 eV), β-Ga_2O_3 (밴드갭 4.8 ~ 4.9 eV), $Al_xGa_{1-x}N$ (밴드갭 3.4 ~ 6.0 eV), 다이아몬드 (밴드갭 5.5 eV) 등이 있다.

주석산화물은 밴드갭 3.6 eV 를 갖는 투명한 반도체로, 투명성과 높은 전기전도성을 동시에 보이는 물질이다. 가시광선 영역에서 97 %의 높은 투과율을 보이며 결정 상태와 도핑에 따라 10^{-4} ~ 10^6 Ω·cm 의 비저항 값을 갖는다. 이러한 특성을 이용하여 투명 전극과 투명 반도체로 쓰이고 있으며, 특히 In_2O_3 의 합금 형태로 태양전지, 평면판 표시 장치 등의

투명전극으로 널리 쓰이고 있다. 물질의 투명성과 넓은 범위의 전기전도도의 공존에 더불어 열· 화학적 안정성을 갖는 주석산화물은 디스플레이 산업에 쓰이고 있는 IGZO 를 대체할 유망한 투명 반도체중 하나이다.

다결정질의 주석산화물과 에피택셜 주석산화물을 이용하여 투명한 박막 트랜지스터를 제작하고 특성을 비교하였다. 유리 기판 위에 반응성 스퍼터링 방법과 어닐링 과정을 거쳐 다결정질 주석산화물을 증착하였고, 145 cm^2/Vs 의 높은 이동도를 보이는 박막 트랜지스터를 제작하였다. 그러나 다결정질 주석산화물을 이용한 박막 트랜지스터는 이력현상과 전압의존성 등의 비이상적인 특성을 보였다. 이러한 문제는 결정 경계에 형성되는 장벽에서 기인한 것으로, 이를 실험적으로 증명하기 위해 에피택셜 주석산화물 박막 트랜지스터를 제작하였다. 에피택셜 주석산화물은 r-평면 사파이어 기판 위에 펄스 레이저 증착 방법을 통해 증착하였다. 에피택셜 주석산화물 박막 트랜지스터는 비교적 낮은 이동도를 보였지만, 다결정질 주석산화물 박막 트랜지스터에서 보인 비이상적인 특성을 보이지 않았다. 이로부터 결정 경계에 생기는 장벽이 다결정질 주석산화물 박막 트랜지스터의 불안정한 소자 특성을 유발하고, 에피택셜 주석산화물 층에 형성되는 관통 전위와 역위상경계가 낮은 이동도의 원인이 되는 것을 알 수 있었다. 이로부터, 다결정질 주석산화물의 상용화를 위해선 결정 경계에 대한 완전한 이해가 선행되어야 함을 알 수있다.

정상 스피넬 산화물인 아연갈륨산화물은 4.6 ~ 5.2 eV 의 초광대역 밴드갭을 갖는 물질로 가시광선 영역 뿐만 아니라 자외선 영역에서도 투명하다. 갈륨산화물 베타 위상과 동일한 갈륨팔면체 회로망을 기반으로 하는 아연갈륨산화물은 사면체배위에 위치하는 아연과 팔면체배위에 위치하는 갈륨 두 개의 양이온을 가지고 있으며, 정상 입방 스피넬 구조를 갖기

때문에, 등방성을 보이며 안정적으로 상을 유지한다. 더불어 높은 전기전도도와 도핑가능성을 갖기 때문에 갈륨산화물 베타 위상보다 뛰어난 특성을 보일것으로 기대된다. 이러한 장점으로부터, 아연갈륨산화물은 하이파워소자와 자외선 투명 소자 분야에 사용 가능한 물질로 주목받고 있다.

아연갈륨산화물은 펄스 레이저 증착 방법을 통해 마그네슘알루미늄산화물 ($MgAl_2O_4$)과 마그네슘산화물 (MgO) 기판의 결에 맞는 에피택셜 층으로 성장되었다. 엑스선 회절과 전자투과현미경을 이용하여 각 기판 위에서의 아연갈륨산화물은 관통 전위와 격자 정수차이로 생기는 전위가 없는 스피넬 구조임을 확인 하였다. 아연갈륨산화물은 양이온 구성 비와 기판에 의한 변형에 따라 다른 구조적·전기적 특성을 보였다. 박막 트랜지스터는 아연/갈륨 비율이 이상적인 값보다 약간 적은 조건에서 장력을 받을 때 가장 높은 이동도 5.4 cm^2/Vs, 4.5 $\times 10^8$ 에 해당하는 큰 점멸비, 0.19 V/de 의 작은 문턱전압이하 스윙 값을 보였다. 박막과 박막 트랜지스터로 확인한 구조적·전기적 특성으로부터, 아연의 빈자리와 갈륨이 아연 자리에 위치하는 결함이 아연갈륨산화물의 지배적인 결함인 것을 알 수 있었다. 이로부터, 아연갈륨산화물의 결함과 변형의 영향에 대해 완전히 이해한다면, 더 높은 이동도를 보이는 아연갈륨산화물 박막 트랜지스터를 구현할 수 있을것으로 기대한다.

주요어: 넓은 밴드갭 산화물 반도체, 주석산화물, 아연갈륨산화물, 박막, 박막 트랜지스터

학 번: 2013-22994